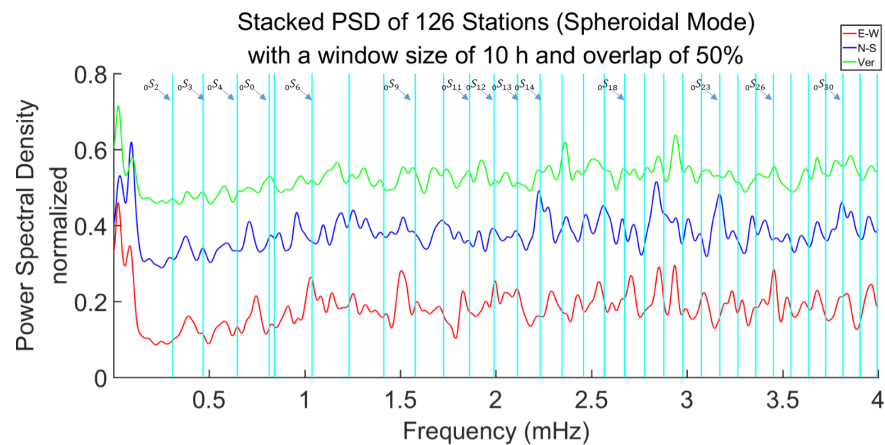


Analysing Normal Modes of the Earth from High-rate GNSS Time Series



Master Thesis

in study program GEOENGINE

University of Stuttgart

Zhongyi Chen

Stuttgart, August 2017

Supervisor: Prof. Dr.-Ing. Nico Sneeuw
University of Stuttgart

Prof. Dr.-Ing. Caijun Xu
Wuhan University

Declaration

I declare that this thesis has been composed solely by myself and that it has not been submitted, in whole or in part, in any previous application for a degree. Except where stated otherwise by reference or acknowledgement, the work presented is entirely my own.

Place, Date *Chengde, August, 2017*

Signature *Zhongyi Chen*

Abstract

Normal modes of the Earth, or Earth's free oscillations, correspond to a global deformation of the Earth that vibrates at different frequencies, like a bell, after a strong excitation, usually an earthquake of magnitude greater than 6.5.

Normal modes of the Earth were first described by Lord Kelvin (Kelvin, 1863) with a computation of the lowest fundamental spheroidal mode ${}_0S_2$ frequency for a homogeneous Earth model (Lognonné and Clévedé, 2002). With the theory and the deployment of the first long-period sensors in the late 1950s, day-scale Earth's free oscillation after large earthquakes has been detected by underground instruments such as strainmeters, gravimeters and seismometers (Benioff et al., 1961) (Dziewonski and Gilbert, 1972) (Mendiguren, 1973).

In the 1960s, since the U.S. military developed the first satellite navigation system, Transit, the era of Global Navigation Satellite System (GNSS) has arrived. Among all navigation satellite systems, Global Positioning System (GPS), operated by the U.S. Department of Defense (DOD), is currently the world's most utilized satellite navigation system.

With the developments of receiver technology and sampling capability, GPS becomes a powerful tool to study long-period Earth deformations such as plate tectonics and post-glacial rebound, or to monitoring short-period and short-duration motion such as waves generated by earthquakes (Bilich et al., 2008).

In recent years, several studies have demonstrated the effective use of GPS in estimating coseismic displacement waveforms induced by an earthquake with accuracies ranging from a few millimeters to a few centimeters.

In these studies, two well-known processing strategies, single Precise Point Positioning (PPP) and Different Positioning (DP), have been used to reduce the latency between earthquake occurrence and coseismic displacement waveforms estimation. In this thesis, a new approach named Variometric Approach for Displacements Analysis Standalone Engine (VADASE) is used to detect the normal modes of the Earth. Then the Welch's PSD estimate is applied to transform the time series into frequency domain.

Several simulations have been performed on synthetic time series to investigate the influence of noise level, sampling rate, time series length, window size and overlapping rate of Welch's method, as well as the influence of stacking.

The experiments on real data show the capability of VADASE time series for detecting normal modes of the Earth with the help of the stacking method. Some fundamental modes with small amplitude are not visible because the SNR is not sufficient to lift the signal out of the noise.

Acknowledgements

I feel much indebted to many people who have instructed and favored me in the thesis work.

First of all, I would like to express my sincere gratitude to my supervisor, Prof. Dr.-Ing. Nico Sneeuw for his invaluable advice and constant encouragement.

I would also like to thank all the teachers who have taught me in the two years, who have helped me enrich and broaden my knowledge.

My thanks also go to Prof. Xu, Prof. Crespi, Dr. Widmer, Mr. Giorgio, Mr. Niu for their informative suggestions and patient guidance in data processing.

Finally, I would like to express my thanks to my family and my friends for their spiritual support during my study.

Contents

Declaration of Authorship	iii
Abstract	v
Acknowledgements	vii
Contents	ix
1 Normal modes of the Earth	1
1.1 Introduction	1
1.2 Normal modes of a SNREI model	2
1.2.1 Spheroidal modes and toroidal modes	3
1.2.2 Degeneracy in SNREI Earth model	4
1.2.3 Splitting of normal modes	6
2 GPS system	9
2.1 Overview	9
2.2 GPS signal	10
2.3 Ephemeris	13
2.4 GPS observation	14
2.4.1 Trilateration	14
2.4.2 Two types of observables	15
2.5 Atmospheric effects	17
2.6 GPS seismology	19
2.6.1 History	19
2.6.2 Difference between GPS and traditional instruments in seismology fields	20
3 GPS positioning	23
3.1 Absolute versus relative positioning	23
3.1.1 GPS absolute positioning	23
3.1.2 Relative positioning	25
3.2 Static versus kinematic positioning	28
3.3 Real-time versus post processing positioning	28
4 GPS data processing	31
4.1 Most used strategies	31
4.1.1 Differential positioning	31
4.1.2 Single Precise Point Positioning	32
4.1.3 Instantaneous positioning	32
4.1.4 The present challenges	32
4.2 The VADASE approach	33
4.2.1 Introduction	33

4.2.2	The variometric 3D displacement estimation model	33
4.2.3	Least squares estimation	37
5	Spectral analysis	41
5.1	Random signal	41
5.2	Power spectral density estimation	42
5.2.1	Definition of power spectral density	42
5.2.2	Periodogram	43
5.2.3	Bartlett's method	44
5.2.4	Welch's method	45
6	Simulations	47
6.1	Synthetic time series	47
6.1.1	Principle	47
6.1.2	Signal-to-noise ratio	48
6.2	Welch's PSD estimation in Matlab	49
6.3	Simulation results and analyses	50
6.3.1	Different levels of SNR	50
6.3.2	Effects of stacking of many stations	50
6.3.3	Different window size and overlap	51
6.3.4	Different sampling rate and time series length	52
7	Experiments on real VADASE time series	55
7.1	Data source	55
7.2	Estimated PSD with Welch's method	56
7.3	Conclusion	59
A	Ionosphere-free linear combination	63
	Bibliography	65

Chapter 1

Normal modes of the Earth

1.1 Introduction

Earth's normal modes, or free oscillations, are standing waves along the surface and radius of the Earth. These standing waves only exist at discrete frequencies and are similar to the different "tones" of musical instruments. Since the amplitudes of the modes are very small, usually less than 1 mm, the normal modes are only observable by precise instruments after a strong excitation like an earthquake of magnitude greater than M_w 6.5.

The study of the Earth's normal modes is fundamental to seismology, as it is a key part of the theory of the Earth's dynamic response to external or internal forces. It also helps to investigate Earth's internal structure, density profile, geodynamics and source properties of earthquakes.

During almost a century, up to 1960, normal modes were only theoretical concepts. Normal modes of the Earth were first described by Kelvin (1863). The lowest fundamental spheroidal mode ${}_0S_2$ frequency for a homogeneous Earth model was computed in his study. This early attempt was followed by a complete description of the normal modes of a spherical nonrotating elastic isotropic (SNREI) Earth in the early works of Rayleigh (1896) and Love (1911). The first computation of normal mode frequencies for realistic models of the Earth (at that time obtained from body wave arrival time data) were performed with a more complete calculation of eigenfrequencies and eigenmodes, and the search for normal mode signatures started in the very late 1950s (Benioff et al., 1959).

The first early observations started from the Chile 1960 earthquake with the theory and the development of the first real long-period sensors, such as strainmeters, tiltmeters, and gravimeters. The analyses of records performed by Benioff et al. (1961), Ness et al. (1961), Alsop et al. (1961), Bolt and Marussi (1962) showed an excellent fit with the theoretical frequencies, as well as splitting related to the rotation of the Earth (Backus and Gilbert, 1961).

After the pioneering work of Backus and Gilbert (1961), most of the attention was given to the effect of elastic lateral variations and ellipticity after 1970. Perturbation theory appeared very rapidly as a tool for the treatment first of the Earth rotation and ellipticity (Dahlen, 1968) and then of the lateral variations in the isolated multiplet case by Zharkov and Lyubimov (1970a,b), Madariaga and Aki (1972). In the next decade, refined perturbation theories were applied: quasi-degenerate theory for the rotation and ellipticity (Dahlen, 1969) and for lateral variations (Woodhouse, 1980).

In parallel with these theoretical and numerical studies, observations and inversions were performed to constrain the lateral variations of the Earth with early work of Jordan (1978) and Silver and Jordan (1981), the latter leading to the discovery of the elastic degree-two pattern of the Earth's mantle (Masters et al., 1982) and of the anomalous splitting of some modes depicting a large sensitivity to the core (Masters and Gilbert, 1981). However, after almost two decades of discussions, a complete explanation of all anomalous modes and of body wave travel times in the core is still lacking.

The first observation of attenuation lateral variation was performed by Romanowicz (1990, 1994) and Roult et al. (1990) in the 1980s and 1990s. The theory of normal modes were also finally refined when Woodhouse and Dahlen (1978) and Valette (1986) completed the theoretical framework for a nonhydrostatic prestressed Earth. The attenuation theory was also developed first in a nonrotating Earth (Lognonné, 1989), and then in a rotating anelastic Earth (Lognonné, 1991).

The last and most recent achievement was in 1998, with the discovery of the permanent excitation of the normal modes of the Earth. Despite an early suggestion of Benioff et al. (1959), normal modes were always sought only after strong excitations. Nawa et al. (1998), Suda et al. (1998), Kobayashi and Nishida (1998) showed that normal modes were in fact permanently excited at the level of the nanogal, too small for their observation on a single record but sufficiently enhanced by stacking of at least one year's signals.

1.2 Normal modes of a SNREI model

Normal modes of a SNREI Earth constitute the basis of normal mode theory, even in an aspherical Earth. They indeed constitute a complete basis of all functions verifying the same boundary and continuity conditions on the spherical surface of the Earth and internal discontinuities respectively, as shown by Valette (1987) in the elastic case. Therefore, normal modes of a spherical Earth can be used to describe the normal modes of all Earth

models with any lateral variations but the same spherical shape and discontinuities.

1.2.1 Spheroidal modes and toroidal modes

The displacements on a vibrating string can be written as:

$$d(x, t) = \sum_{j=0}^{\infty} A_j \sin\left(\frac{j\pi x}{L}\right) \cos(\omega_j t), \quad (1.1)$$

where x is the horizontal coordinate, A is the amplitude, $\sin\left(\frac{j\pi x}{L}\right)$ is the eigenfunction, j is the mode number, as shown in figure 1.1.

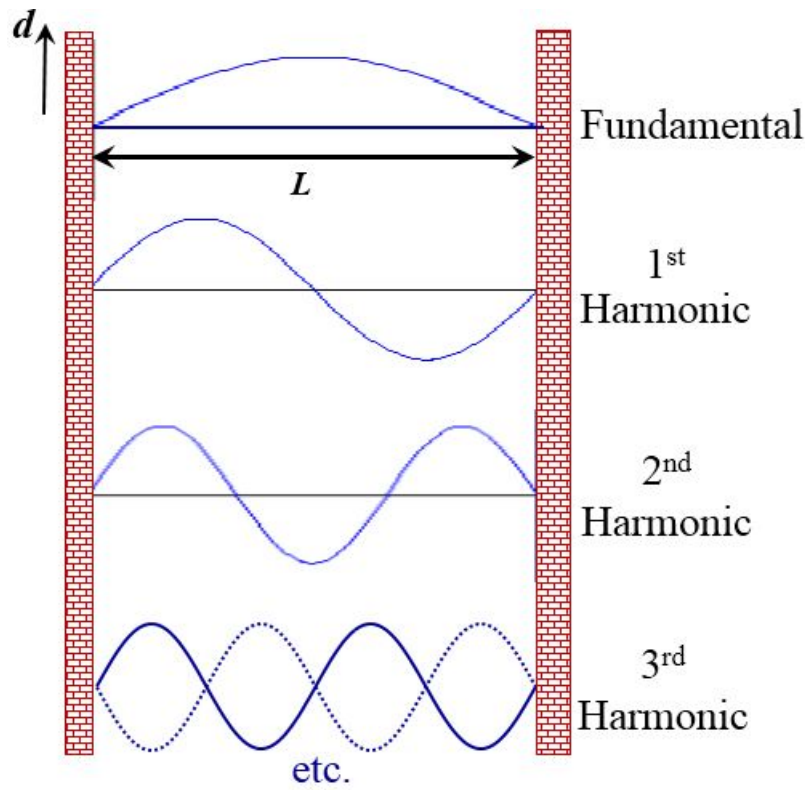


FIGURE 1.1: **Vibration on a string** (by Michel Van Camp, Royal Observatory of Belgium)

Similarly, the vibration on the sphere can be written as:

$$u(r, \theta, \phi) = \sum_{n=0}^{\infty} \sum_{l=0}^{\infty} \sum_{m=-l}^l {}_n A_l^m {}_n Y_l(r) X_l^m(\theta, \phi) e^{i n \omega_l^m t}, \quad (1.2)$$

where ${}_n Y_l$ and X_l^m are the radial and surface eigenfunctions.

Applying spherical harmonics, the free vibrations of a nonrotating elastic sphere can be separated into two groups: the spheroidal modes:

$$u^S(r, \theta, \phi) = \sum_{n=0}^{\infty} \sum_{l=0}^{\infty} \sum_{m=-l}^l {}_n A_l^m [{}_n U_l(r) R_l^m(\theta, \phi) + {}_n V_l(r) S_l^m(\theta, \phi)] e^{i {}_n \omega_l^m t}, \quad (1.3)$$

and the toroidal modes:

$$u^T(r, \theta, \phi) = \sum_{n=0}^{\infty} \sum_{l=0}^{\infty} \sum_{m=-l}^l {}_n A_l^m {}_n W_l(r) T_l^m(\theta, \phi) e^{i {}_n \omega_l^m t}. \quad (1.4)$$

Here n is the radial order, which indicates the number of nodes along the radius of the Earth (also called the overtone number), while l and m (angular and azimuthal order) determine the pattern of displacement on a spherical surface (see figure 1.2). $n = 0$ corresponds to the lowest frequency mode of harmonic degree l and is termed as a “fundamental mode”. Again, V_l, U_l, W_l , functions of r , are the radial eigenfunctions, while R_l^m, S_l^m, T_l^m are the surface eigenfunctions.

The spheroidal modes (P-SV; changes in volume) are denoted by ${}_n S_l^m$ and are sensitive to compressional and shear wavespeed as well as density. Both radial and tangential motions are involved. By contrast, the toroidal modes (SH; rotation or shear; no change in volume) are denoted by ${}_n T_l^m$ and are sensitive only to shear wavespeed. There is no radial component of toroidal modes.

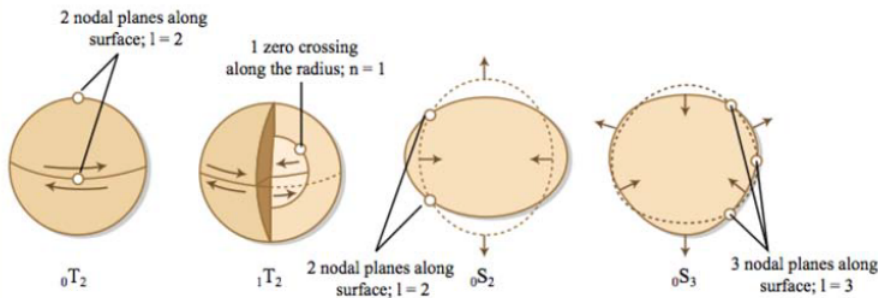


FIGURE 1.2: Spheroidal and toroidal motion diagrams (by MIT OCW)

1.2.2 Degeneracy in SNREI Earth model

In eqns. (1.2) to (1.4), for each l there exist $2l + 1$ modes (also called multiplets). Each individual mode determined by n, l, m is called singlet. For example, for $l = 0$, there is only one mode, i.e., $m = 0$; for $l = 1$, there are three modes corresponding to $m = 0, \pm 1$.

If a SNREI Earth model, e.g., PREM, is applied, for each n and l the multiplets can be degenerated because different azimuthal orders have the same frequency. Some of the fundamental spheroidal and toroidal modes of PREM model are listed in table 1.1 (Masters and Widmer, 1995).

TABLE 1.1: Fundamental normal modes in PREM model

Spheroidal mode	f^{PREM} [μHz]	Toroidal mode	f^{PREM} [μHz]
${}_0S_2$	309.28	${}_0T_2$	379.17
${}_0S_3$	468.56	${}_0T_3$	586.16
${}_0S_4$	647.07	${}_0T_4$	765.66
${}_0S_0$	814.31	${}_0T_5$	928.24
${}_0S_5$	840.42	${}_0T_6$	1078.83
${}_0S_6$	1038.21	${}_0T_7$	1220.70
${}_0S_7$	1231.79	${}_0T_8$	1356.11
${}_0S_8$	1413.51	${}_0T_9$	1486.61
${}_0S_9$	1578.28	${}_0T_{10}$	1613.26
${}_0S_{10}$	1726.47	${}_0T_{11}$	1736.85
${}_0S_{11}$	1862.42	${}_0T_{12}$	1857.94
${}_0S_{12}$	1990.37	${}_0T_{13}$	1976.99
${}_0S_{13}$	2112.94	${}_0T_{14}$	2094.36
${}_0S_{14}$	2231.40	${}_0T_{15}$	2210.34
${}_0S_{15}$	2346.38	${}_0T_{16}$	2325.19
${}_0S_{16}$	2458.22	${}_0T_{17}$	2439.09
${}_0S_{17}$	2567.12	${}_0T_{18}$	2552.22
${}_0S_{18}$	2673.30	${}_0T_{19}$	2664.71
${}_0S_{19}$	2776.98	${}_0T_{20}$	2776.67
${}_0S_{20}$	2878.37	${}_0T_{21}$	2888.20
${}_0S_{21}$	2977.73	${}_0T_{22}$	2999.37
${}_0S_{22}$	3075.27	${}_0T_{23}$	3110.25
${}_0S_{23}$	3171.26	${}_0T_{24}$	3220.90
${}_0S_{24}$	3265.89	${}_0T_{25}$	3331.35
${}_0S_{25}$	3359.38	${}_0T_{26}$	3441.64
${}_0S_{26}$	3451.91	${}_0T_{27}$	3551.80
${}_0S_{27}$	3543.65	${}_0T_{28}$	3661.86
${}_0S_{28}$	3634.76	${}_0T_{29}$	3771.84
${}_0S_{29}$	3725.34	${}_0T_{30}$	3881.75
${}_0S_{30}$	3815.52	${}_0T_{31}$	3991.62
${}_0S_{31}$	3905.40		
${}_0S_{32}$	3995.04		

1.2.3 Splitting of normal modes

However, the real Earth is of course not a SNREI Earth model. The degeneracy will be removed because of rotation of the Earth (Coriolis), ellipticity and lateral heterogeneity (see figure 1.3). In general, each singlet within a multiplet will have a slightly different frequency. This phenomenon is called “splitting”(Masters and Widmer, 1995).

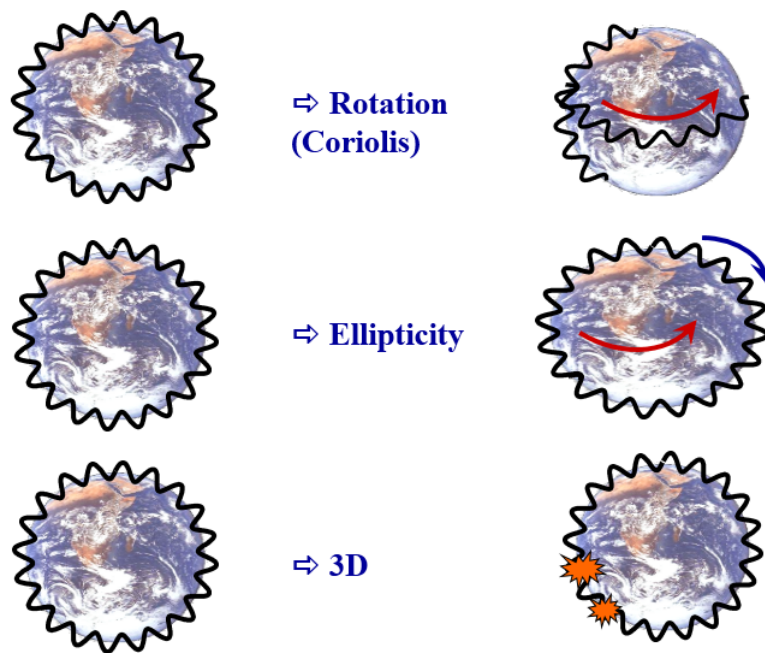


FIGURE 1.3: Splitting of normal modes caused by rotation, ellipticity and heterogeneity (by Michel Van Camp, Royal Observatory of Belgium)

Free oscillation *per se* is the interference of traveling waves. Intuitively, the rotation of the Earth causes the waves in the direction of rotation to travel faster. Similarly, the waves from pole to pole run a shorter path than along the equator because of the ellipticity. The lateral heterogeneity will also accelerate or slow down the waves. All effects mentioned above result in the waves on one path to take more time than another path. This will lead to the splitting of normal modes.

The splitting can be obviously detected in the frequency domain. It was firstly found by Benioff et al. (1961) after the great Chile earthquake of 1960. Figure 1.4 shows an example of data and theoretical amplitude spectrum computed for the spherically symmetric PREM model (Dziewonski and Anderson, 1981). Take the mode ${}_1S_4$ for example, it is split into two peaks in the data spectrum, which is not seen in the theoretical spectrum.

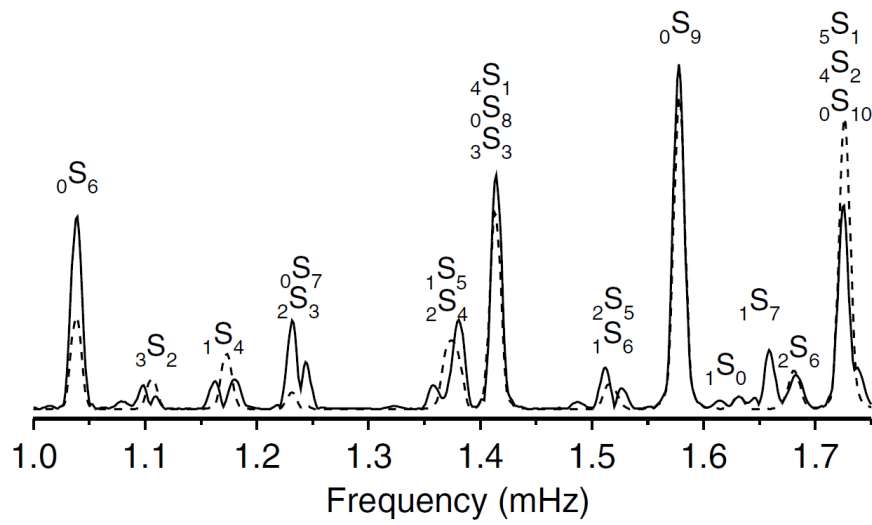


FIGURE 1.4: Splitting of normal modes

Data (solid line) and PREM synthetic spectrum (dashed line) for the vertical component recording at station ANMO following the great Sumatra event of 2004

Chapter 2

GPS system

2.1 Overview

Global Positioning System (GPS) is a satellite-based radionavigation system developed and operated by the U.S. Department of Defense (DOD). GPS permits land, sea, and airborne users to determine their three-dimensional position, velocity, and time 24 hours a day, in all weather condition, anywhere in the world where there is an unobstructed line of sight to at least four GPS satellites.

GPS consists of three segments: space, control, and user.

- **The Space Segment** consists of a minimum of 24 operational satellites in 6 circular orbits 20 200 km above the earth at an inclination angle of 55° with an 11 h 58 min period (see figure 2.1). Although it is not a stated requirement, typically the satellites are spaced in primary orbital slots so that at any time a minimum of 6 satellites will be in view to users anywhere in the world.

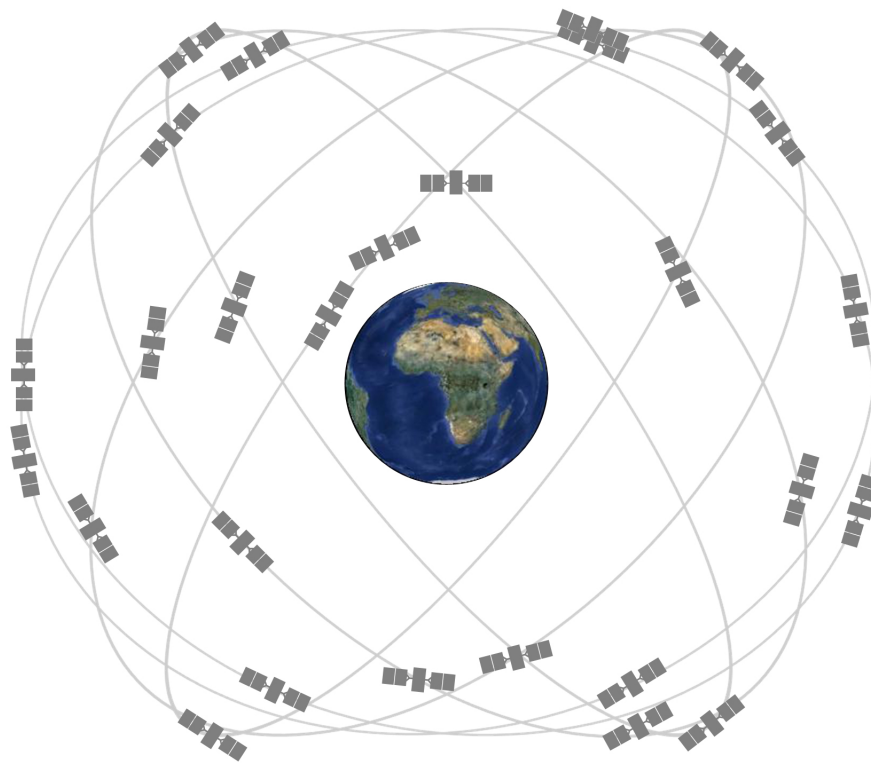


FIGURE 2.1: Space segment (constellation)

(source: <http://www.gps.gov/systems/gps/space/>)

- **The Control Segment** consists of a master control station in Colorado Springs, with five monitor stations and three ground antennas located throughout the world. The monitor stations track all GPS satellites in view and collect ranging information from the satellite broadcasts. The monitor stations send the information they collect from each of the satellites back to the master control station, which computes extremely precise satellite orbits. The information is then formatted into updated navigation messages for each satellite. The updated information is transmitted to each satellite via the ground antennas, which also transmit and receive satellite control and monitoring signals.
- **The User Segment** consists of the receivers, processors, and antennas that allow land, sea, or airborne operators to receive the GPS satellite broadcasts and compute their precise position, velocity and time.

2.2 GPS signal

GPS satellites (called space vehicles in the GPS interface specification documents) broadcast microwave signals to enable GPS receivers on or near the Earth's surface to determine location, velocity and time.

GPS signals include carrier signal, ranging code which is used to measure the distance to the satellite, and navigation messages.

The carrier frequency can be described as a sinusoidal phenomenon, while the ranging code is a periodic sequence or rectangular pulse, where the amplitude changes pseudo randomly between 0 and 1 (see figure 2.2). Finally, the navigation message is generated.

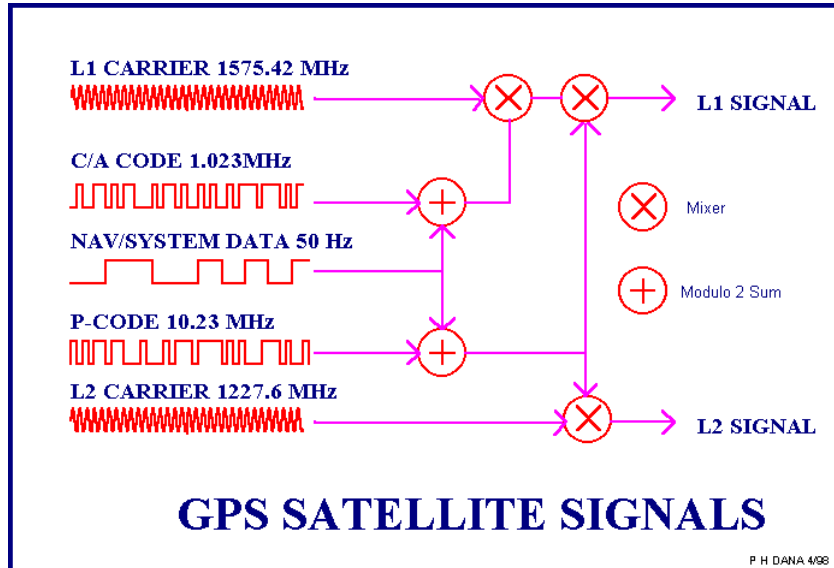


FIGURE 2.2: GPS satellite signals
(by Peter H. Dana, Department of Geography, University of Texas at Austin)

Carrier signal

The oscillators on board the satellites generate a signal with fundamental frequency f_0 equal to 10.23 MHz. Two coherent carrier signals denoted L_1 and L_2 are derived from f_0 by multiplying the fundamental frequency by 154 and 120 respectively (see table 2.1).

TABLE 2.1: Carrier frequency for the GPS navigation signals

Carrier wave	Factor (* f_0)	Frequency [MHz]	Wavelength [cm]
L_1	154	1575.42	19.03
L_2	120	1227.60	24.42

Ranging code

The carrier signals are phase modulated with two Pseudo Random Noise (PRN) codes (see table 2.2): the C/A code (coarse/acquisition) and the P code (precise). Both codes are pseudo-random sequences of 0 and 1, but

they cannot be truly random, since they are generated with a mathematical algorithm. The code chipping rate of the C/A code is 1/10 of the fundamental frequency f_0 , while for the P code it is equal to the fundamental frequency.

TABLE 2.2: The GPS binary code

Code name	Description	Frequency [MHz]
C/A	Coarse/acquisition code for civil use, modulates L_1	1.023
P	Precise code, modulates both L_1 and L_2	10.23

Navigation message

The navigation message is modulated on both carriers at 50 bit/s. The whole message contains 25 pages (or frames) of 30 s each, forming the master frame that takes 12.5 min to be transmitted. Every frame is divided into 5 sub-frames of 6 s each and every sub-frame consists of 10 words, with 30 bit per word (see figure 2.3). Sub-frames 4 and 5 have 25 different pages. The navigation message essentially contains:

- (1) broadcast ephemeris which is used to calculate the position of each satellite in orbit;
- (2) parameters of the satellite clock offset;
- (3) parameters of the ionosphere;
- (4) almanac data which contain the status of the entire satellite constellation.

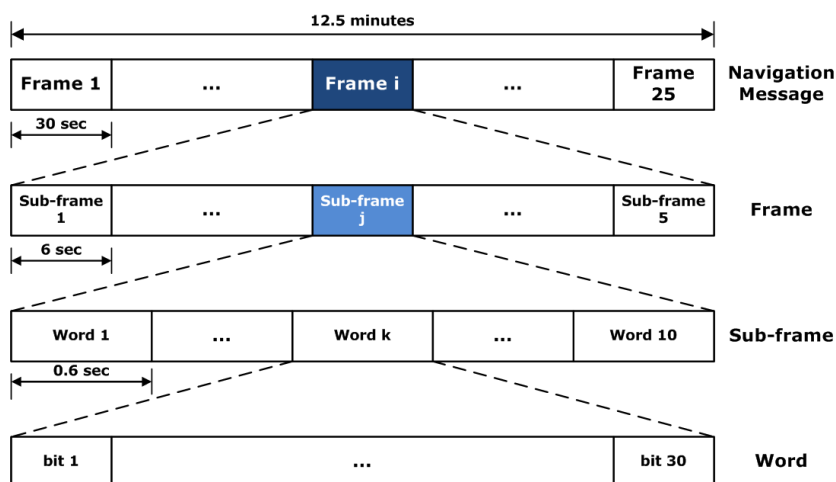


FIGURE 2.3: GPS Navigation message

(source: http://www.navipedia.net/index.php/File:Navigation_Message.png)

2.3 Ephemeris

A GPS receiver requires almanac and ephemeris data to provide the necessary location information requested by a user. Almanac data contains coarse orbital parameters from all global navigation satellites and it can be used by and transmitted to other navigation satellites. Almanac data is not very precise and it can be several months old. On the contrary, ephemeris data is very precise because of the fact that it uses clock correction technology. For precise navigation information, ephemeris data is used by global positioning systems. It only stays valid for approximately 30 min and it is broadcast by satellites every 30 s. Every navigation satellite broadcasts its own ephemeris data only.

Considering exclusively the force of the Earth's gravity as a dominant force on GPS satellite in an inertial reference system, and taking the Earth as a radially symmetric sphere, the satellite orbit can be thought as an ellipse according to Keplerian motion. In fact, there are also other forces that affect the satellite orbits, for this reason the orbit is not perfectly a Keplerian motion but a disturbed one. Hence, the final description of the orbit is based on the *quasi* Keplerian model which needs 16 numeric parameters instead of 6 of the Keplerian model (see figure 2.4).

There are also many sets of ephemeris data available: broadcast ephemeris, precise ephemeris, rapid precise ephemeris and ultra-rapid ephemeris. The accuracy of the orbit is inversely proportional to the latency time:

- broadcast ephemeris has an accuracy of about 160 cm;
- precise ephemeris with a latency of 14 days has an accuracy of few centimeters;
- rapid ephemeris has an accuracy of about 5 cm;
- ultra-rapid ephemeris has an accuracy of 10 cm.

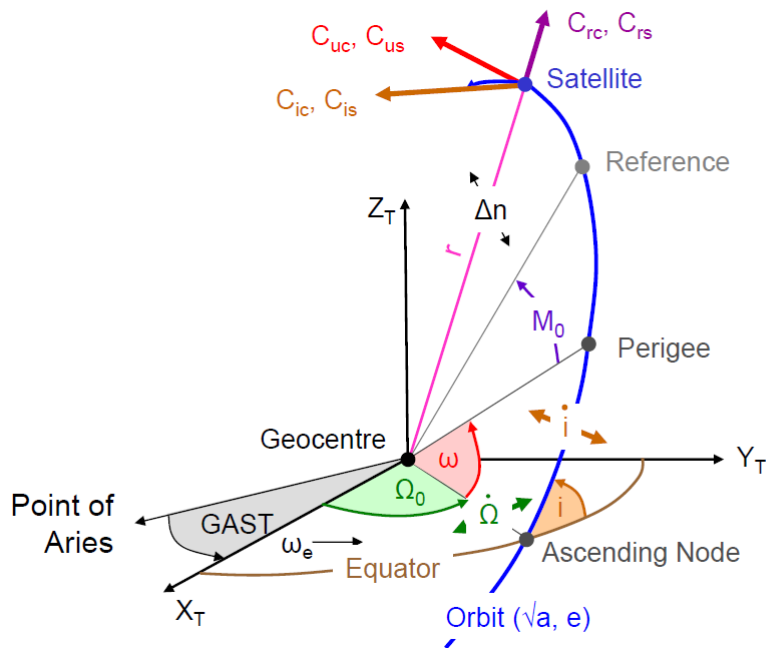


FIGURE 2.4: Broadcast ephemeris parameters
(source: <http://netclass.csu.edu.cn/jpkc2007/csu/02gpsjpkch/jiao-an/4.1.htm>.)

2.4 GPS observation

GPS positioning works on two basic mathematical concepts. The first is called trilateration, which literally means positioning from three distances. The second concept is the fact that the traveled distance can be determined by the speed of travel and traveled time.

$$\text{Distance} = \text{Speed} \times \text{Time}$$

In GPS positioning the speed of travel is the rate is how fast the radio signal travels, which is equal to the speed of light. Time is determined by how long it takes for a signal to travel from the GPS satellite to a GPS receiver. With a known rate and a known time, the distance between satellite and receiver can be solved.

2.4.1 Trilateration

GPS positioning can be compared to trilateration (illustrated in figure 2.5). Both techniques rely exclusively on the measurement of distances to fix positions. The distances, called ranges in GPS, are measured to satellites orbiting in nearly circular orbits at a nominal altitude of about 20 000 km above the Earth. Instead of there being three lines intersecting at the unknown

point in terrestrial trilateration, there are at least four observations in GPS because four unknown, coordinates in three direction, and time have to be calculated.

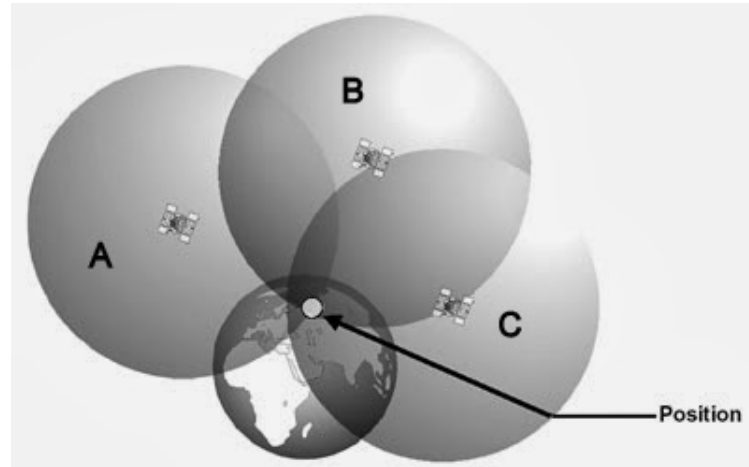


FIGURE 2.5: Trilateration

(source: <http://www.physics.org/article-questions.asp?id=55>)

2.4.2 Two types of observables

The word observable is used throughout GPS literature to indicate the signals whose measurement yields the range between the satellite and the receiver. In GPS there are two types of observables: the code pseudorange and the carrier phase. The latter is the basis of the techniques used for high-precision GPS surveys. On the other hand, the code pseudorange can serve applications when virtually instantaneous point positions are required or relatively low accuracy will suffice.

- **Code pseudorange**

The pseudorange is a measure of the distance between the satellite and the receiver's antenna. The foundation of code pseudoranges is the correlation of code carried on a modulated carrier wave received from a GPS satellite with a replica of that same code generated in the receiver. At first the receiver identifies the satellite by its C/A code and then the time difference between receiver signal and receiver-generated signal is measured as shown in eqn. (2.1).

$$\Delta T_r^s = (t_r + \delta t_r) - (t^s + \delta t^s) = (t_r - t^s) + (\delta t_r - \delta t^s) = \tau_r^s + (\delta t_r - \delta t^s), \quad (2.1)$$

where subscript r and superscript s denote the receiver and satellite, respectively. t^s and t_r are considered as the true emission time and reception

time of the GPS signal. δt^s and δt_r are the satellite and receiver clock errors. The GPS satellite clock error term δt^s is indeed known through GPS satellite navigation message. The clock error is usually modeled by polynomials of time.

Then the code pseudorange is obtained by multiplying the time shift ΔT_r^s by the speed of light c :

$$R_r^s = c\tau_r^s + (\delta t_r - \delta t^s)c = \rho_r^s + c(\delta t_r - \delta t^s), \quad (2.2)$$

where the range ρ_r^s is the geometric distance, which corresponds to the distance between the position of the satellite at the epoch t^s and the position of the antenna of the receiver at epoch t_r . In other words, the range ρ_r^s is calculated from the true signal travel time.

- **Carrier phase**

A more precise observable than the code pseudorange is the phase of the received carrier with respect to the phase generated by an oscillator in the GPS receiver. This observable is obtained by measuring the phase difference between one of the two carrier waves (L_1 or L_2) and the sinusoidal signal, with the same frequency, generated by the oscillator on the receiver. For the specified L_1 frequency the wavelength is 19.03 cm and for the L_2 is 24.42 cm. This ensures the high accuracy positions or high accuracy velocities at the centimeter or centimeter per second level respectively.

The phase equation can be written as:

$$\Phi_r^s(t) = \Phi_r(t) - \Phi^s(t_0) = \Phi_r(t) - \Phi^s(t - \tau_r^s), \quad (2.3)$$

where $\Phi_r^s(t)$ is the phase difference between the carrier signal of the satellite and the generated sinusoidal signal by the oscillator of the receiver. $\Phi_r(t)$ denotes the phase of the receiver at the epoch of the observation, and $\Phi^s(t_0)$ denotes the phase generated in the satellite at the epoch of data transmission. τ_r^s is again the time difference between the signal emission time and reception time.

Stopping the Taylor series at the first order at term $\Phi^s(t - \tau_r^s)$, eqn. (2.4) becomes:

$$\Phi_r^s(t) = \Phi_r(t) - \Phi^s(t) + \tau_r^s f + N_r^s(t). \quad (2.4)$$

The instantaneous fractional beat phase ($\Phi_r(t) - \Phi^s(t)$) can be precisely measured, while $N_r^s(t)$, the integer number of wavelengths between the satellite and the receiver during the travel time of the signal, is unknown. $N_r^s(t)$ is also called integer ambiguity, and will remain the same if the tracking is

continued without loss of lock. Once the integer ambiguity is fixed, the phase difference between the satellite and the receiver can be determined.

The phases $\Phi_r(t)$ and $\Phi^s(t)$ can be also written as:

$$\Phi_r(t) = \Phi(t) + \delta t_r(t)f, \quad (2.5)$$

$$\Phi^s(t) = \Phi(t) + \delta t^s(t)f. \quad (2.6)$$

Substituting the above two equations into eqn. (2.4), it becomes:

$$\Phi_r^s(t) = \tau_r^s f + N_r^s(t) + (\delta t_r(t) - \delta t^s(t))f. \quad (2.7)$$

Multiplying eqn. (2.7) by the wavelength λ , the range between the satellite and the receiver can be expressed in eqn. (2.8):

$$\begin{aligned} L_r^s(t) &= c\tau_r^s + \lambda N_r^s(t) + c(\delta t_r(t) - \delta t^s(t)) \\ &= \rho_r^s + \lambda N_r^s(t) + c(\delta t_r(t) - \delta t^s(t)). \end{aligned} \quad (2.8)$$

This is the final phase pseudorange and it differs from the code pseudorange by the term $\lambda N_r^s(t)$.

2.5 Atmospheric effects

Both systematic errors (biases) and random noise affect the code pseudoranges and phase pseudoranges. The error sources can be classified into three groups (see table 2.3)

TABLE 2.3: GPS error source and value

Group	Error source	Value [m]
Satellite	Clock bias	1.5 to 3.6
	Orbit errors	<1
Signal propagation	Ionospheric refraction	5.0 to 7.0
	Tropospheric refraction	0.5 to 0.7
	Multipath	0.6 to 1.2
Receiver	Noise	0.3 to 0.4
	Clock bias	0.3 to 1.5

The orbit errors, effect of multipath, and receiver noise can be considered as a random noise in the observation, which is denoted as ε . While the effect of ionospheric and tropospheric refraction can be determined by different models.

- **Ionospheric delay**

The ionosphere is that part of the upper atmosphere where free electrons occur in sufficient density to have an appreciable influence on the propagation of radio frequency electromagnetic waves. It extends from about 50 km to 1000 km above the Earth's surface and is the first part of the atmosphere that the GPS signal encounters as it leaves the satellite.

The primary effect of the ionosphere on GPS signal is to change the signal propagation speed as compared to the speed in vacuum. The signal modulation (the ranging code and navigation message) is delayed, while the carrier phase is advanced by the same amount.

The magnitude of these delays is determined by the state of the ionosphere (density and stratification) at the moment the signal passes through. This density is often described as total electron content (TEC), a measure of the number of free electrons in a column through the ionosphere with a cross-sectional area of 1 m^2 . The higher the electron density the larger the delay of the signal, but the delay is by no means constant. The ionospheric delay changes slowly through a daily cycle. It is usually least between midnight and early morning and most around local noon or a little after. The TEC also varies spatially, e.g., the ionospheric delay for a satellite varied from one meter at zenith to several meters at low elevation angle.

Fortunately, for dual frequency receivers, the ionospheric delay can be eliminated by using two signals with different frequency. That is because the ionosphere is a dispersive media and the GPS signals refraction depends on the frequency.

- **Tropospheric delay**

Troposphere is the atmospheric layer placed between the Earth's surface and an altitude of about 60 km. It is composed of dry gases and water vapor, which lengthen the propagation path due to the refraction. The magnitude of the resulting signal delay depends on the temperature, pressure, humidity as well as the transmitter and receiver antennas location. Typically, the tropospheric delay varies from about 2.5 m in the zenith direction to 10 m to 15 m for low satellite elevation angle (Grewal et al., 2007).

The main feature of the troposphere is that it is a non dispersive media with respect to electromagnetic waves up to 15 GHz, i.e., the tropospheric effects are not frequency dependent for the GPS signals. Hence, the code pseudorange and carrier phase pseudorange are affected by the same delay. Therefore, the tropospheric delay cannot be measured by dual frequency measurements (as it is done with the ionosphere); model or differential positioning must be used to reduce the error.

The refractive index of the troposphere can be divided in hydrostatic (dry gases) and wet (water vapor) components, which contribute about 90% and 10% of the total. The hydrostatic component can be modeled from surface pressure and temperature using the laws of the ideal gases. while the wet component is more unpredictable and difficult to model because there is considerable spatial and temporal variation of water vapor in the atmosphere. Nevertheless, fortunately, most of the tropospheric delay (about 90%) comes from the predictable hydrostatic component.

With respect to above considerations, new terms must be added to the equations of code pseudorange and carrier phase pseudorange:

$$R_r^s = \rho_r^s + c(\delta t_r - \delta t^s) + T_r^s + I_r^s + \varepsilon, \quad (2.9)$$

$$L_r^s = \rho_r^s + \lambda N_r^s + c(\delta t_r - \delta t^s) + T_r^s - I_r^s + \varepsilon, \quad (2.10)$$

where T_r^s and I_r^s denote the tropospheric delay and ionospheric delay respectively. Tropospheric path delay is the same for code and carrier signal in contrast to the ionosphere, as explained above. For this reason, the term I_r^s in eqns. (2.9) and (2.10) has a different sign.

2.6 GPS seismology

Since the early stages of development, it became clear that the extensive deployment of GPS stations all over the world had the potential to improve many tasks in geodesy and geodynamics. From that time, the stacked GPS time series acted as an invaluable tool to monitor long-period large-scale geophysical and geodynamical events such as crustal deformation, sea-level changes, post-glacial crustal rebound and coseismic and postseismic deformations.

2.6.1 History

Observations from an array of continuous GPS receiver were firstly used to measure the coseismic displacement caused by the M_w 7.2 Landers, California earthquake in 1992 (Herring and Hudnut, 1993). However, the much larger, even though temporary, displacements caused by the elastic waves radiated from the earthquake source could not be observed because of the low data acquisition rate and the low temporal resolution of coordinates estimation (Nikolaidis et al., 2001).

In the late 1990s, the important advances achieved in GPS receiver technology, together with the increased data storage capability made it possible to acquire and store GPS observations with much higher sampling rates (up to 20 Hz). Since then, the application of GPS had been widened, such as using the receiver as a seismometer to observe the waveforms caused by large magnitude events.

Moreover, Ge (1999) used two Leica CRS1000 GPS receivers operating in Real-Time Kinematic (RTK) mode with a sampling rate of 10 Hz to test the feasibility of using a GPS receiver as a seismometer in order to directly measure large displacements.

Recently, Mitsui and Heki (2012) prove that the dense GPS array can truly detect both spheroidal and toroidal fundamental modes in three dimensional displacements using data after the 2011 Tohoku great earthquake.

2.6.2 Difference between GPS and traditional instruments in seismology fields

Inertial seismometers are electromechanical systems that measure the relative motions between an internal mass and the instrument frame (Nikolaidis et al., 2001). Such systems can obtain velocity or acceleration signals when they are directly perturbed. For this reason, seismic data must be integrated, once for velocity and twice for acceleration records in order to recover displacements. The integration is often a source of errors and has the potential to amplify noise and to distort the true signal. On the other hand, GPS receivers record the pseudorange measurements to the satellites and the position of the receiver antenna should be estimated from these ranges. Besides, seismic instruments can saturate or clip with sufficiently large ground motion so that the instruments do not record the full amplitude of local velocity or acceleration. By contrast, GPS observations do not saturate in amplitude because the observation capability of the receiver has no limits. Moreover, seismometers operate in the presence of gravity, and the tilt of the instrument can produce artificial horizontal acceleration, while GPS instruments are not affected in this way.

However, the natural disadvantage of GPS instruments is that their sensitivity to seismic ground motion is not as good as that of seismic instruments. In this respect, Larson (2009) suggested that GPS could most effectively contribute to seismology if used as a strong motion instrument. Actually, GPS instruments can be consistently used to measure large displacements with high accuracy because they record the receiver displacements as primary results without any integration.

Furthermore, a notable difference lies in the reference frame of the two types instruments. Traditional seismic instruments record signal directly in an inertial reference frame whereas GPS is able to recover displacements with respect to a global reference frame.

In conclusion, the contribution of GPS is an effective push forward to seismology towards the global coverage and the better assessment of large earthquakes and seismic events.

Chapter 3

GPS positioning

When using GPS technology to obtain the position of a point, there are different methods to choose from: absolute or relative positioning; static or kinematic positioning; real-time or post processing positioning.

3.1 Absolute versus relative positioning

Positioning with GPS can be performed by either of two ways: absolute positioning or relative positioning.

Absolute positioning, also called point positioning or single point positioning, employs only one GPS receiver that measures the code pseudorange to determine the user's position instantaneously, as long as four or more satellites are visible at the receiver. GPS absolute positioning is used mainly when a relatively low accuracy is required. This includes recreation applications and low accuracy navigation. However, once the integer ambiguity is known, high accuracy can be achieved by using carrier phase measurement, such as the precise point positioning (PPP).

GPS relative positioning, however, employs two or more GPS receivers simultaneously tracking the same satellites. If the receivers track at least four common satellites, a positioning accuracy level of centimeter can be obtained with the phase observation. Hence, GPS relative positioning is used for high accuracy applications such as surveying and mapping, GIS, and precise navigation.

3.1.1 GPS absolute positioning

GPS absolute positioning involves only one receiver at the user's location to collect data from at least four satellites, in order to calculate the user's position. Absolute positioning can be done in two different ways: real-time positioning or static point positioning, which will be discussed later. It is

worth to mention that for the real-time positioning only code observations can be used.

According to eqn. (2.9), there are only four unknowns, i.e., three dimensional coordinates of the receiver and the clock error, at each epoch, independent on the number of satellites. For this reason, four simultaneously measured pseudoranges are required. In stead for the phase observations, as shown in the eqn. (2.10), the number of unknowns depends on the number of satellites. at each epoch of acquisition there are above mentioned four unknowns plus one integer ambiguity N_r^s for each satellite. So the absolute positioning with carrier phase for a single epoch is only possible when the integer ambiguities are resolved first. For such a reason the code ranges are usually used for the absolute positioning.

- **Absolute positioning with code pseudorange**

The concept of absolute positioning is illustrated in figure 3.1

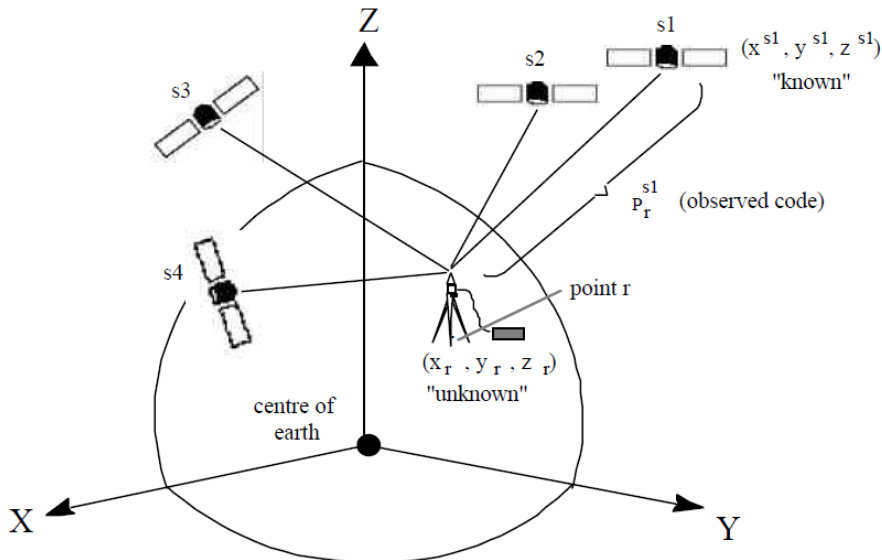


FIGURE 3.1: Absolute positioning
(source: "GPS Positioning Guide", 3rd edition)

In the figure, s_1, s_2, s_3, s_4 represent four different satellites being tracked. The positions of these satellites are referenced to the center of the Earth in the Cartesian coordinate frame and are denoted as (x^s, y^s, z^s) . The coordinates of the receiver, the unknown point, as referenced to the Earth center, are (x_r, y_r, z_r) .

The code pseudorange at an epoch t can be defined according to eqn. (2.9):

$$R_r^s(t) = \rho_r^s(t) + c(\delta t_r(t) - \delta t^s(t)) + T_r^s(t) + I_r^s(t) + \varepsilon. \quad (3.1)$$

The term $R_r^s(t)$ is the measured code pseudorange between the satellites and the receiver. It is worth noting that eqn. (3.1) is a non linear equation because of the term $\rho_r^s(t)$, which is the geometric distance between the satellites and the observing point. $\rho_r^s(t)$ can be expressed as:

$$\rho_r^s(t) = \sqrt{(x^s(t) - x_r)^2 + (y^s(t) - y_r)^2 + (z^s(t) - z_r)^2}. \quad (3.2)$$

Hence, at first the observation equations of the code pseudorange must be linearized using the Bancroft solution (Bancroft, 1985).

For the above equations, there are different unknowns for each epoch of observation: the three site coordinates, the clock error of the satellite and the receiver clock error. Fortunately, the satellite clock error can be corrected by applying the satellite correction in the broadcast navigation message.

For static point positioning, the unknowns are: the three coordinates of the observing site, which are always the same, and the receiver clock bias, that changes every epoch. Denoting the number of satellites and the number of epochs with n_s and n_t respectively. Then the number of unknown is $3 + n_t$, and the sufficient condition to solve the system can be represented as:

$$n_s n_t \geq 3 + n_t.$$

3.1.2 Relative positioning

The concept of relative positioning is illustrated in figure 3.2. Instead of determining the coordinates of one point on the Earth with respect to the satellite, the position of the point is determined with respect to a known point, which is generally stationary. Higher accuracy can be achieved because the combination of observations from two receivers cancels out common GPS satellite and receiver clock errors and reduces other error sources.

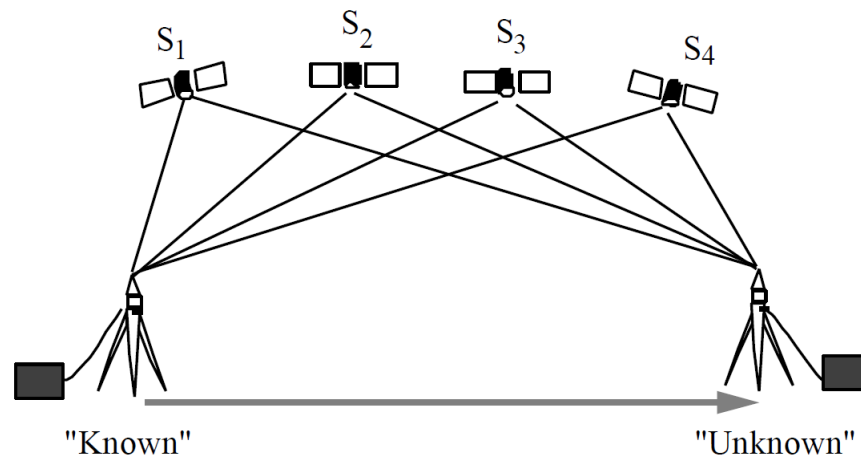


FIGURE 3.2: Relative positioning
(source: "GPS Positioning Guide", 3rd edition)

Different linear combinations can be used to realize relative positioning as shown in figure 3.3.

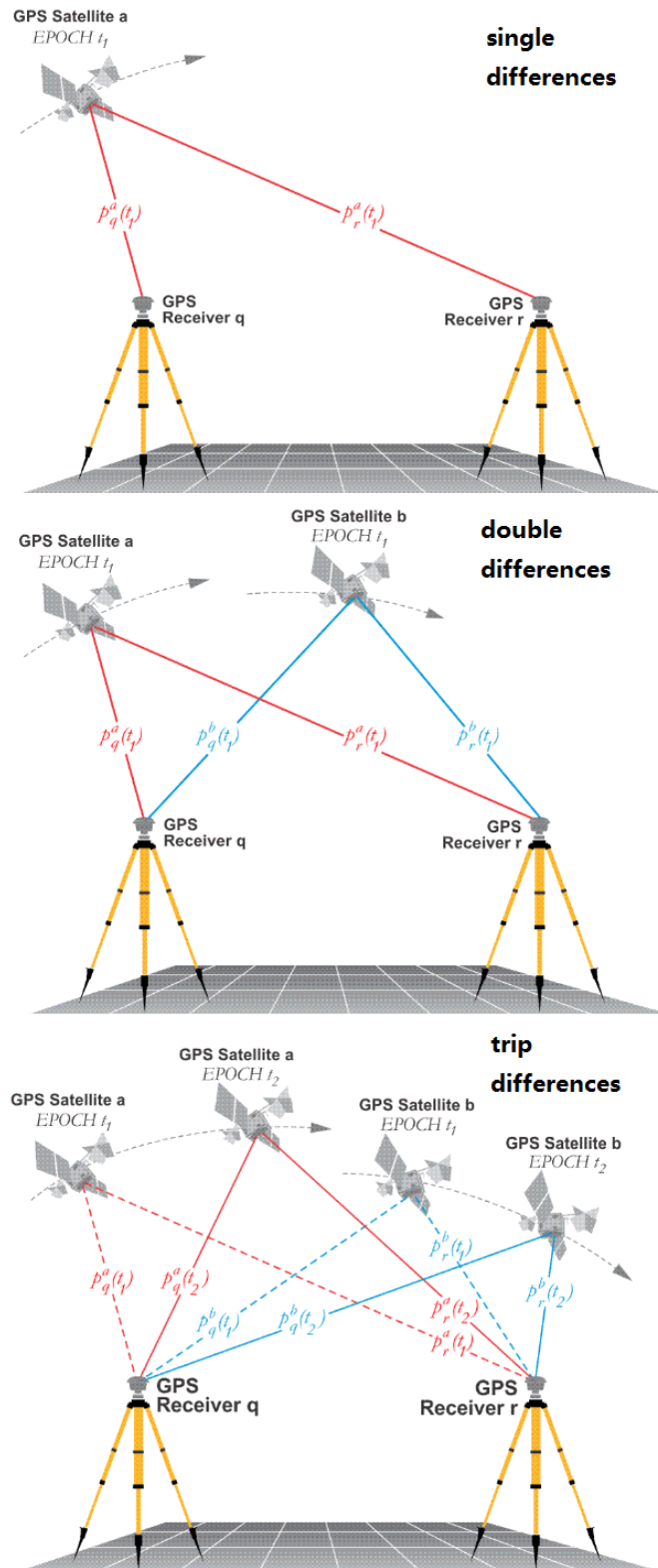


FIGURE 3.3: Different linear combinations for relative positioning

(source: <https://www.e-education.psu.edu/geog862/node/1727>)

- **Single differences** corresponds to across-receiver differences in general. Two receivers and one satellite are involved. The satellite clock error can be canceled out. If the two receivers are within, say 20 km, the ionospheric and tropospheric delay can be also reduced. Single differencing can also be applied across satellites to eliminate the receiver clock error, or across epochs to eliminate the initial integer ambiguity.
- **Double differences** corresponds to the across-receiver and across-satellite difference. Two receivers and two satellites are involved. It is done by differencing single differences between two satellites. Hence, the receiver clock error is removed.
- **Triple difference** corresponds to across-receiver, across-satellite and across-time differences. It is done by differencing double differences between two epochs. It is able to cancel out the integer ambiguity if the tracking is continuous.

3.2 Static versus kinematic positioning

GPS positioning can also be categorized as static or kinematic. In static positioning, the GPS receiver is required to be stationary whereas in kinematic positioning the receiver collects GPS data while moving. Both static and kinematic positioning can be applied for absolute or relative positioning. Recently, the accuracy of static positioning at the millimeter level is achieved. This level of accuracy has made GPS useful for static positioning applications, such as the study of crustal deformations related to earthquake and volcanic processes. By contrast, kinematic positioning is widely used in navigation.

3.3 Real-time versus post processing positioning

GPS positions may be attained through real-time or post processing. In real-time processing, the receiver position is computed almost instantaneously on site. While in post processing, the measurements are collected in the field and processed at a later time to obtain the results. Each of these modes has some advantages and some disadvantages.

The first advantage of the real-time mode is that the results as well as the accuracy measures (or quality control) are obtained while in the field. This is especially important for real-time kinematic (RTK) surveying, as the user

would not store the displayed coordinates unless the ambiguity parameters are shown to be fixed integer values and centimeter-level accuracy is achieved. This leads to a higher productivity compared with the post processing mode, as only enough GPS data to obtain a fixed solution is collected. In addition, processing the GPS data is done automatically in the field by the built-in software. This means that no post processing software training is required. The user also saves the time spent in data processing.

There are, however, some advantages in the post processing mode as well. The first of these is that more accurate results are generally obtained with the post processing mode. One reason for this is more flexibility in editing and cleaning of the collected GPS data. In some cases, the input parameters, such as the base station coordinates or the antenna height, may contain some errors, which lead to errors in the computed rover coordinates. These errors can be corrected in the post processing mode, while they cannot be completely corrected in the real-time mode.

Chapter 4

GPS data processing

4.1 Most used strategies

Up to date, the following two approaches have been adopted for GPS seismology: differential positioning and single Precise Point Positioning. Co-seismic displacements have been estimated with a post-processing approach using various scientific softwares, e.g., GAMIT/GLOBK, GIPSY and Bernese. High quality products (orbits, clocks, Earth orientation parameters) are provided by the International GNSS Service (IGS) or by NASA's Jet Propulsion Laboratory (JPL). These products are freely available and have a latency period ranging from 17 h to 41 h (the so called rapid products) to 12 d to 18 d (the so called precise products).

4.1.1 Differential positioning

There are essentially two ways in which measurements from two receivers are used to account for biases, and hence improve accuracy:

- Each set of measurements at a receiver are independently used to derive a position which is in error by more or less the same amount. This is the differential GPS (DGPS) procedure implemented for precise navigation applications using pseudorange data;
- Differencing measurements between receivers leads to an observable that is essentially free of biases (or at least substantially reduced if the receivers are not too far away). This is the GPS surveying mode of differential positioning using carrier phase data.

Differential positioning requires at least two receivers set up at two stations (usually one is known) to collect satellite data simultaneously in order to determine coordinate differences. This method will position the two stations relative to each other and can provide the accuracies required for land surveying.

4.1.2 Single Precise Point Positioning

Single Precise Point Positioning is a high precise mode of GPS positioning developed by NASA's JPL. It can provide around 1 cm accuracy with single receiver and without any ground control.

The basic PPP idea is that precise orbits and clock information are precisely given from some other sources, hence the position can be determined accurately.

The major difference between DGPS and PPP is that the measurements and corrections of the PPP technique are free from the reference receiver. Unlike in DGPS, common mode errors do not cancel in PPP. The coordinates of the target station computed by using the PPP technique contain also errors which need to be removed. These satellite dependent errors including geometrical dilution of precision (GDOP), clock error and orbit error, propagation errors including ionospheric and tropospheric delay, multipath and receiver dependent errors including receiver clock error, antenna phase center variation and measurement uncertainty.

4.1.3 Instantaneous positioning

Additionally, the long latency in both DGPS and PPP has been overcome by the technique referred to as instantaneous positioning (Bock et al., 2000). This technique is based on differential positioning and allows the fundamental resolution of integer cycle phase ambiguities using single epoch dual-frequency pseudorange and carrier phase observations. Hence, instantaneous positioning provides a precise independently computed position for each observation epoch, at the sampling rate of the receiver. However, in order to achieve the mentioned accuracy of 1 cm in real-time, instantaneous positioning requires both a complex and continuously linked infrastructure (GPS permanent network) with a maximum average inter-station distance of up to several tens to a few hundreds of kilometers.

4.1.4 The present challenges

The biggest challenge in normal modes detection is the accuracy of the time series, since the amplitudes of normal modes are usually less than 1 mm. Although the DP strategy can reach to an accuracy of mm, it only provides a relative coseismic displacement, which is the displacement with respect to (at least) one reference station due to the adoption of differential positioning approach. A strong earthquake may involve the entire area covered by the permanent GPS network, including the reference station. For such a reason,

co-seismic displacements in a global reference frame are not available since even the reference station is influenced by a displacement. While the PPP strategy can only reach to an accuracy level of 2 cm to 4 cm, it can detect the normal modes of the Earth with a stacking among vast stations.

Considering the shortcomings of the above mentioned strategies, during the Real Time GPS Science Requirements Workshop held in September, 2007 in Leavenworth (Washington, USA) the goal of achieving 1 cm real-time GNSS co-seismic displacement accuracies in the global reference frame, within the three minutes following an earthquake, was adopted (Blewitt et al., 2009).

4.2 The VADASE approach

4.2.1 Introduction

The VADASE approach, abbreviation of Variometric Approach for Displacements Analysis Stand-Alone Engine is a new approach for estimating co-seismic displacements in the global reference frame in real-time. It is able to use a single receiver to obtain real-time results, with accuracies ranging from few centimeters up to a couple of decimeters.

VADASE is developed at the Geodesy and Geomatics Division (DICEA, Department of Civil, Building and Environmental Engineering) of the University of Rome La Sapienza. Since October 2010, VADASE was recognized as a simple and effective approach for high-frequency real-time co-seismic displacement waveform estimation.

The potentialities of VADASE were internationally recognized for the first time immediately after the tremendous earthquake in Japan (March 11, 2011 M_w 9.0) when the researchers provided the first waveforms results among the scientific community (Branzanti et al., 2013).

4.2.2 The variometric 3D displacement estimation model

VADASE is an algorithm able to estimate, on the basis of carrier phase observations and broadcast orbits, the velocity of a GNSS receiver between two observations epochs. The receiver displacements waveforms, for short intervals (few minutes), can be retrieved from the estimated velocities by simple integration.

The first step to describe the so called “variometric” algorithm is the standard raw carrier phase observation equation (Hofmann-Wellenhof et al.,

2007) expressed in length units. Consider the error coming from multipath effect, the noise and other effects, eqn. (2.10) can be expressed as:

$$\lambda\Phi_r^s = \rho_r^s + c(\delta t_r - \delta t^s) + T_r^s - I_r^s + \lambda N_r^s + p_r^s + m_r^s + \epsilon_r^s, \quad (4.1)$$

where Φ_r^s is the carrier phase observation of the receiver (r) with respect to the satellite (s); λ is the carrier phase wavelength; p_r^s is the sum of other effects (such as, relative effects, phase center variation, phase wind-up); m_r^s and ϵ_r^s respectively represent the multipath effect and the noise. It is worth to note that all the terms of eqn. (4.1), but the initial phase ambiguity, are related to observation epoch (t). Here, both the time and the frequency dependency are omitted for simplicity.

If dual frequency GPS observation free from cycle slips are considered, eqn. (4.1) can be different in time between two consecutive epochs ($t, t+1$). Thus, the ionospheric term may be canceled to the second order by applying a so-called ionosphere-free combination (see Appendix A) to the time single-difference, which becomes the ionosphere-free time single-difference equation:

$$\begin{aligned} & \alpha[\lambda\Delta\Phi_r^s(t, t+1)]_{L1} + \beta[\lambda\Delta\Phi_r^s(t, t+1)]_{L2} \\ & = \Delta\rho_r^s(t, t+1) + c(\Delta\delta t_r(t, t+1) - \Delta\delta t^s(t, t+1)) \\ & + \Delta T_r^s(t, t+1) + \Delta p_r^s(t, t+1) + \Delta m_r^s(t, t+1) + \Delta\epsilon_r^s(t, t+1), \end{aligned} \quad (4.2)$$

where $\alpha = f_{L1}^2/(f_{L1}^2 - f_{L2}^2)$ and $\beta = -f_{L2}^2/(f_{L1}^2 - f_{L2}^2)$ are the standard coefficients of the ionosphere-free combination, $\Delta m_r^s(t, t+1)$ and $\Delta\epsilon_r^s(t, t+1)$ are the multipath effect and the noise in the time single-difference, respectively. It is worth to note that using this convention, the value of t is always an integer and represents the time of the observation in units equal to the inverse of the frequency of the observation.

If we hypothesize that the receiver is fixed in an Earth centered Earth fixed reference frame (ECEF), the term $\Delta\rho_r^s(t, t+1)$ depends on the change of the geometric range due to satellite's orbital motion and Earth's rotation ($[\Delta\rho_r^s(t, t+1)]_{\text{OR}}$). However, it is also dependent on the variation of the solid Earth tide and ocean loading ($[\Delta\rho_r^s(t, t+1)]_{\text{EtOl}}$) (McCarthy and Petit, 2003). Hence, we have:

$$\Delta\rho_r^s(t, t+1) = [\Delta\rho_r^s(t, t+1)]_{\text{OR}} + [\Delta\rho_r^s(t, t+1)]_{\text{EtOl}}. \quad (4.3)$$

On the other hand, if we hypothesize that the receiver underwent a 3D displacement $\Delta\vec{\xi}_r(t, t+1)$ in an ECEF reference frame during the interval $(t, t+1)$, the term $\Delta\rho_r^s(t, t+1)$ also contain the effect of $\Delta\vec{\xi}_r$ projected along the line-of-sight, which is observed over two consecutive epochs (t and $t+1$) if high-rate (≥ 1 Hz) observations are utilized. Therefore, it is possible to write:

$$\begin{aligned}\Delta\rho_r^s(t, t+1) &= [\Delta\rho_r^s(t, t+1)]_{\text{OR}} + [\Delta\rho_r^s(t, t+1)]_{\text{EtOI}} + [\Delta\rho_r^s(t, t+1)]_{\text{D}} \\ &= [\Delta\rho_r^s(t, t+1)]_{\text{OR}} + [\Delta\rho_r^s(t, t+1)]_{\text{EtOI}} + \vec{e}_r^s \cdot \Delta\vec{\xi}_r(t, t+1),\end{aligned}\quad (4.4)$$

where \vec{e}_r^s is the unit vector from the satellite to the receiver at epoch t .

Here, it is important to note that the displacement $\Delta\vec{\xi}_r(t, t+1)$, if divided by the interval which is observed over two consecutive epochs $(t, t+1)$, is equal to the (mean) velocity over the interval $(t, t+1)$ itself. Therefore, the displacement $\Delta\vec{\xi}_r(t, t+1)$, which is expressed in length units, is basically equivalent to a velocity, and it will be referred to as “velocity” in the following discussion. To summarize, it is possible to say that the GPS receiver is being used as a velocimeter.

The tropospheric term $\Delta T_r^s(t, t+1)$ represents variation of the tropospheric delay during the interval $(t, t+1)$. This term is modeled by computing the Zenith Tropospheric Delay (ZTD) (i.e. $T_r^s(Z_r^s = 0)$) according to the Saastamoinen model (Saastamoinen, 1972). Using the standard atmosphere as defined by Liljequist and Cehak (2013) and applying the mapping function included in Saastamoinen model, the tropospheric delay can be written as follows:

$$T_r^s(Z_r^s(t)) = \frac{0.00277}{\cos(Z_r^s(t))} \left[P + \left(\frac{1255}{T} + 0.05 \right) e_w - \tan^2 Z_r^s(t) \right], \quad (4.5)$$

where Z_r^s is the zenith angle of the satellite with respect to the receiver, the atmospheric pressure (P) and the partial water vapor pressure (e_w) are given in millibar, the temperature (T) is given in degree Kelvin and the resulting tropospheric delay is obtained in meter.

Given the definition of the tropospheric delay variation, inserting eqn. (4.4) in eqn. (4.2) and simplifying the notation by omitting the epochs $(t, t+1)$,

yields to:

$$\begin{aligned} \alpha[\lambda\Delta\Phi_r^s]_{L1} + \beta[\lambda\Delta\Phi_r^s]_{L2} &= [\Delta\rho_r^s]_{\text{OR}} + [\Delta\rho_r^s]_{\text{EtOI}} + \vec{e}_r^s \cdot \vec{\Delta\xi}_r \\ &+ c(\Delta\delta t_r - \Delta\delta t^s) + \Delta T_r^s + \Delta p_r^s + \Delta m_r^s + \Delta\epsilon_r^s, \end{aligned} \quad (4.6)$$

which can be rewritten in the form of the so defined variometric equation as follows:

$$\begin{aligned} \alpha[\lambda\Delta\Phi_r^s]_{L1} + \beta[\lambda\Delta\Phi_r^s]_{L2} &= (\vec{e}_r^s \cdot \vec{\Delta\xi}_r + c\Delta\delta t_r) \\ &+ ([\Delta\rho_r^s]_{\text{OR}} - c\Delta\delta t^s + \Delta T_r^s) \\ &+ ([\Delta\rho_r^s]_{\text{EtOI}} + \Delta p_r^s) + \Delta m_r^s + \Delta\epsilon_r^s, \end{aligned} \quad (4.7)$$

where:

- $\alpha[\lambda\Delta\Phi_r^s]_{L1} + \beta[\lambda\Delta\Phi_r^s]_{L2}$ are the time single-difference ionosphere-free observations;
- $(\vec{e}_r^s \cdot \vec{\Delta\xi}_r + c\Delta\delta t_r)$ are terms containing the four unknowns parameters (the 3D velocity $\Delta\xi_r$ and the receiver clock error variation $\Delta\delta t_r$);
- $([\Delta\rho_r^s]_{\text{OR}} - c\Delta\delta t^s + \Delta T_r^s)$ is the largest part of the known term that can be computed on the basis of known orbits and clocks and for the chosen tropospheric model;
- $([\Delta\rho_r^s]_{\text{EtOI}} + \Delta p_r^s)$ is an additional much smaller known term that can be computed with proper models for all of the considered effects;
- Δm_r^s and $\Delta\epsilon_r^s$ are the multipath effect and the noise term, as described previously.

Eqn. (4.12) represents the functional model of the least squares estimation problem. It is well known that low elevation observations are usually noisier, such that the observations are weighted by the squared cosine of the satellite zenith angle (Z_r^s) (Dach et al., 2007), as follows:

$$w = \cos^2(Z_r^s). \quad (4.8)$$

The least squares estimation of the 3D velocity is based upon the entire set of variometric eqn. (4.12), which can be written for two generic consecutive epochs ($t, t + 1$). The number of variometric equations obviously depends on the number of satellites which are common to the two epochs. At least four satellites are necessary to estimate the four unknown parameters for each consecutive epoch pair.

4.2.3 Least squares estimation

First, let us consider the simplified functional model that relates the u unknowns and the n observations:

$$\mathbf{y} = \mathbf{A}\mathbf{x}, \quad (4.9)$$

where $\mathbf{y}_{n \times 1}$ is the observations vector, $\mathbf{A}_{n \times u}$ is the design matrix containing the coefficients for the unknowns, and $\mathbf{x}_{u \times 1}$ is the vector with the u unknown parameters. Considering eqn. (4.9), a consistent solution with respect to the parameters reads as:

$$\mathbf{x} = \mathbf{A}^{-1}\mathbf{y}, \quad (4.10)$$

where observations should be independent in order for \mathbf{A}^{-1} to be non singular. Here, it is important to note that, in order for the inverse matrix \mathbf{A}^{-1} to exist, matrix \mathbf{A} should be square and regular. In case the number of observations is greater than the number of unknowns the problem becomes overdetermined and $n - u$ is referred to as the redundancy. Redundant problems are usually solved using least squares estimation method.

Generally, observations are affected by noise and uncertainty which are assumed to be Gaussian normally distributed with zero mean and to have a covariance matrix denoted as Σ_ν (e.g. $\nu \sim N(0, \Sigma_\nu)$). Eqn. (4.9) yields:

$$\mathbf{y} = \mathbf{A}\mathbf{x} + \nu, \quad (4.11)$$

which corresponds to the general form of a Gauss-Markov model. Here, the functional model is expressed as:

$$E[\mathbf{y}] = \mathbf{A}\mathbf{x}, \quad E[\nu] = 0, \quad (4.12)$$

and the stochastic model reads as:

$$D[\mathbf{y}] = \Sigma_y = \sigma_0^2 \mathbf{Q}_y, \quad (4.13)$$

where $E[\cdot]$ is the expectation operator and $D[\cdot]$ is the dispersion operator which describes the covariance matrix of the observations Σ_y . σ_0^2 is referred to as the a priori variance of unit weight and it is often assumed to be 1, \mathbf{Q}_y

corresponds to the cofactor matrix. The inverse of the cofactor matrix is denoted as the weight matrix:

$$\mathbf{W} = \mathbf{Q}_y^{-1}. \quad (4.14)$$

Since the observations are assumed to be independent from one another, the weight matrix becomes diagonal (i.e. the terms expressing the correlation between the observations are equal to zero). The strategy to solve eqn. (4.11) is to constrain the sum of the squares of the residuals to be minimum:

$$\boldsymbol{\nu}^T \mathbf{W} \boldsymbol{\nu} = (\mathbf{y} - \mathbf{A}\mathbf{x})^T \mathbf{W} (\mathbf{y} - \mathbf{A}\mathbf{x}) = \text{minimum}. \quad (4.15)$$

The vector of unknowns is estimated with

$$\hat{\mathbf{x}} = (\mathbf{A}^T \mathbf{W} \mathbf{A})^{-1} \mathbf{A}^T \mathbf{W} \mathbf{y} = \mathbf{N}^{-1} \mathbf{y} \quad (4.16)$$

where \mathbf{N} denotes the normal matrix. Any bias or outlier in the observations will deteriorate the models (i.e. mathematical and stochastic) and result into faulty parameters and faulty statistical values (Hofmann-Wellenhof et al., 2007). The estimated values are used to retrieve the residuals:

$$\hat{\boldsymbol{\nu}} = \mathbf{y} - \mathbf{A}\hat{\mathbf{x}}, \quad (4.17)$$

which are then used to estimate the a posteriori variance of unit weight:

$$\sigma^2 = \frac{\hat{\boldsymbol{\nu}}^T \mathbf{W} \hat{\boldsymbol{\nu}}}{n - u}. \quad (4.18)$$

A practical example of least squares estimation technique applied to VADASE algorithm is further described. Let assume that n satellites are viewed by the receiver at both epochs t and $t + 1$, the terms of eqn. (4.11) display as follows:

$$\mathbf{y}_{n \times 1} = \begin{bmatrix} \alpha[\lambda\Delta\Phi_r^1]_{L1} + \beta[\lambda\Delta\Phi_r^1]_{L2} \\ \alpha[\lambda\Delta\Phi_r^2]_{L1} + \beta[\lambda\Delta\Phi_r^2]_{L2} \\ \vdots \\ \alpha[\lambda\Delta\Phi_r^n]_{L1} + \beta[\lambda\Delta\Phi_r^n]_{L2} \end{bmatrix} \quad \mathbf{A}_{n \times 4} = \begin{bmatrix} e_{rX}^1 & e_{rY}^1 & e_{rZ}^1 & 1 \\ e_{rX}^2 & e_{rY}^2 & e_{rZ}^2 & 1 \\ \vdots & \vdots & \vdots & \vdots \\ e_{rX}^n & e_{rY}^n & e_{rZ}^n & 1 \end{bmatrix}$$

$$\mathbf{x}_4 = \begin{bmatrix} \Delta X \\ \Delta Y \\ \Delta Z \\ \Delta \delta t_r \end{bmatrix} \quad \mathbf{b}_n = \begin{bmatrix} [\Delta \rho_r^1]_{\text{OR}} + \Delta T_r^1 - c\Delta \delta t^1 \\ [\Delta \rho_r^2]_{\text{OR}} + \Delta T_r^2 - c\Delta \delta t^2 \\ \vdots \\ [\Delta \rho_r^n]_{\text{OR}} + \Delta T_r^n - c\Delta \delta t^n \end{bmatrix}$$

where n is the number of observations and $u = 4$ is the number of unknowns. To be consistent with the exposition of the variometric algorithm given in eqn. (4.12), it is possible to introduce the vector \mathbf{b} containing the so called known terms and to reformulate the general problem as:

$$\mathbf{y} = \mathbf{A}\mathbf{x} + \mathbf{b} + \boldsymbol{\nu}. \quad (4.19)$$

The observations are assumed to be uncorrelated and are weighted by the squared cosine of the satellite zenith angle (Z_r^s):

$$\mathbf{W}_{n \times n} = \begin{bmatrix} \cos^2(Z_r^1) & 0 & \cdots & 0 \\ 0 & \cos^2(Z_r^2) & \cdots & 0 \\ \vdots & \vdots & \ddots & \vdots \\ 0 & 0 & \cdots & \cos^2(Z_r^n) \end{bmatrix}$$

The least squares estimation of the unknowns is finally given as:

$$\hat{\mathbf{x}} = (\mathbf{A}^T \mathbf{W} \mathbf{A})^{-1} \mathbf{A}^T \mathbf{W} (\mathbf{y} - \mathbf{b}). \quad (4.20)$$

Chapter 5

Spectral analysis

Spectral analysis considers the problem of determining the spectral content (i.e., the distribution of power over frequency) of a time series from a finite set of measurements, by means of either nonparametric or parametric approaches.

For the nonparametric approach, the studied signal is applied to a bandpass filter with a narrow bandwidth, which is swept through the frequency band of interest, and the filter output power divided by the filter bandwidth is used as a measure of the spectral content of the input to the filter. The parametric approach is to postulate a model for the data, which provides a means of parameterizing the spectrum, and to thereby reduce the spectral estimation problem to that of estimating the parameters in the assumed model.

In seismology, the spectral analysis of the signals recorded prior to and during a seismic event (such as a volcano eruption or an earthquake) gives useful information on the ground movement associated with such events and may help in analyzing and predicting them.

Parametric methods may offer more accurate spectral estimates than the nonparametric ones in the cases where the data indeed satisfy the model assumed by the former methods. However, in the more likely case that the data do not satisfy the assumed models, the nonparametric methods may outperform the parametric ones owing to the sensitivity of the latter to model misspecification. This has motivated renewed interest in the nonparametric approach to spectral estimation.

5.1 Random signal

Signals can be divided into two main categories: deterministic and random. The term random signal is used primarily to denote signals, which have a

random in its nature source. Many real-world signals can be characterized as being random (from the observer's viewpoint). Generally speaking, this means that the variation of such a signal outside the observed interval cannot be determined exactly. It is only possible to make probabilistic statements about that variation. The mathematical device to describe such a signal is that of a random sequence which consists of an ensemble of possible realizations, each of which has some associated probability of occurrence. Of course, from the whole ensemble of realizations, usually only one realization of the signal can be realized.

When applying frequency-domain techniques to the analysis of the realization of a random signal, the natural approach is to Fourier transform the signals. However, unfortunately, the Fourier transform of a stochastic signal does not, strictly speaking, exist because it has infinite signal energy. But a random signal usually has infinite average power and, therefore, can be characterized by an average power spectral density (PSD).

5.2 Power spectral density estimation

5.2.1 Definition of power spectral density

First, let us assume a discrete-time signal $\{y(t); t = 0, \pm 1, \pm 2, \dots\}$ to be a sequence of random variables with zero mean:

$$E\{y(t)\} = 0 \quad \text{for all } t. \quad (5.1)$$

The autocovariance sequence (ACS) or covariance function of $y(t)$ can be defined as:

$$r(k) = E\{y(t)y^*(t-k)\}, \quad (5.2)$$

where the symbol $(\cdot)^*$ denotes the complex conjugate of a scalar variable or the conjugate transpose of a vector or matrix. $r(k)$ is usually assumed to depend only on the lag between the two samples averaged.

The above two assumptions (5.1) and (5.2) imply that $y(t)$ is a second-order stationary sequence (also known as wide-sense stationary).

First definition

Then the PSD is defined (Stoica and Moses, 2005) as the discrete-time Fourier transform (DTFT) of the covariance sequence:

$$\phi(\omega) = \sum_{k=-\infty}^{\infty} r(k)e^{-i\omega k}. \quad (5.3)$$

The inverse transform which recovers $r(k)$ from given $\phi(\omega)$ is:

$$r(k) = \frac{1}{2\pi} \int_{-\pi}^{\pi} \phi(\omega)e^{i\omega k} d\omega. \quad (5.4)$$

Second definition

The second definition PSD is:

$$\phi(\omega) = \lim_{N \rightarrow \infty} E \left\{ \frac{1}{N} \left| \sum_{t=1}^N y(t)e^{-i\omega t} \right|^2 \right\}. \quad (5.5)$$

This definition is equivalent to (5.3) under the assumption that the covariance sequence $r(k)$ decays sufficiently rapidly, so that

$$\lim_{N \rightarrow \infty} \frac{1}{N} \sum_{k=-N}^N |k||r(k)| = 0. \quad (5.6)$$

The equivalence of eqns. (5.5) and (5.3) can be proved as follows with a double summation formula:

$$\begin{aligned} \lim_{N \rightarrow \infty} E \left\{ \frac{1}{N} \left| \sum_{t=1}^N y(t)e^{-i\omega t} \right|^2 \right\} &= \lim_{N \rightarrow \infty} \frac{1}{N} \sum_{t=1}^N \sum_{s=1}^N E\{y(t)y^*(s)\}e^{-i\omega(t-s)} \\ &= \lim_{N \rightarrow \infty} \frac{1}{N} \sum_{\tau=-(N-1)}^{N-1} (N - |\tau|)r(\tau)e^{-i\omega\tau} \\ &= \sum_{\tau=-\infty}^{\infty} r(\tau)e^{-i\omega\tau} - \lim_{N \rightarrow \infty} \frac{1}{N} \sum_{\tau=-(N-1)}^{N-1} |\tau|r(\tau)e^{-i\omega\tau} \\ &= \phi(\omega) \end{aligned} \quad (5.7)$$

5.2.2 Periodogram

The periodogram method relies on the definition (5.5) of the PSD. Neglecting the expectation and the limit operation in eqn. (5.5), which cannot be

performed when the only available information on the signal consists of the samples $y(t)$ ($t = 1, \dots, N$). Then the periodogram method can be expressed as:

$$\hat{\phi}_p(\omega) = \frac{1}{N} \left| \sum_{t=1}^N y(t) e^{-i\omega t} \right|^2. \quad (5.8)$$

In practice it is not possible to evaluate $\hat{\phi}_p(\omega)$ over a continuum of frequencies. Hence, the frequency variable must be sampled for the purpose of computing $\hat{\phi}_p(\omega)$. The most commonly used frequency sampling scheme is:

$$\omega = \frac{2\pi}{N} n, \quad n = 0, \dots, N-1 \quad (5.9)$$

Then the evaluation of $\hat{\phi}_p(\omega)$ at the frequency samples in eqn. (5.9) basically reduces to the computation of the following discrete Fourier transform:

$$Y(n) = \sum_{t=1}^N y(t) e^{-i \frac{2\pi}{N} nt}, \quad n = 0, \dots, N-1 \quad (5.10)$$

However, the periodogram is an inconsistent spectral estimator because if $y(t)$ is a random variable, then $y(n)$ is a random variable too. Furthermore, the fact that the periodogram values $\hat{\phi}_p(\omega)$ are uncorrelated (for large N values) makes the periodogram exhibit an erratic behavior (similar to that of a white noise realization). These facts constitute the main limitations of the periodogram approach to PSD estimation (Stoica and Moses, 2005). Hence several modified periodogram-based methods are presented to decrease the variance of the estimated spectrum at the expense of increasing its bias (hence, decreasing the averaged spectral resolution).

5.2.3 Bartlett's method

The basic idea of the Bartlett method (Bartlett, 1948, 1950) is to reduce the large fluctuations of the periodogram by splitting up the available sample of N observations into $L = N/M$ subsamples of M observations each, and then average the periodograms obtained from the subsamples for each value of ω . Let

$$y_j(t) = y((j-1)M + t), \quad t = 1, \dots, M; j = 1, \dots, L \quad (5.11)$$

denote the observations of the j th subsample, and let

$$\hat{\phi}_j(\omega) = \frac{1}{M} \left| \sum_{t=1}^M y_j(t) e^{-i\omega t} \right|^2 \quad (5.12)$$

denote the corresponding periodogram. Then the Bartlett spectral estimation is given by:

$$\hat{\phi}_B(\omega) = \frac{1}{L} \sum_{j=1}^L \hat{\phi}_j(\omega). \quad (5.13)$$

Since the Bartlett method operates on data segments of length M , the resolution should be $1/M$. Hence, the spectral resolution of the Bartlett method is reduced by a factor L , compared to the resolution of the original periodogram method. In return for this reduction in resolution, the Bartlett method also has a reduced variance. It can be proved that the Bartlett method reduces the variance of the periodogram by the same factor L .

5.2.4 Welch's method

The Welch method (Welch, 1967) is obtained by refining the Bartlett method in two respects. First, the data segments in the Welch method are allowed to overlap. Second, each data segment is windowed before computing the periodogram. Mathematically, the Welch method can be described as follows. Let

$$y_j(t) = y((j-1)K + t), \quad t = 1, \dots, M; j = 1, \dots, S \quad (5.14)$$

denote the j th data segment. $(j-1)K$ is the starting point for the j th sequence of observations. If $K = M$, then the sequences do not overlap and we get the sample splitting used by the Bartlett method (which leads to $S = L = N/M$ data subsamples). However, the value recommended for K in the Welch method is $K = M/2$, in which case $S \simeq 2M/N$ data segments (with 50% overlap between successive segments) are obtained.

The window periodogram corresponding to $y_j(t)$ is computed as:

$$\hat{\phi}_j(\omega) = \frac{1}{MP} \left| \sum_{t=1}^M v(t) y_j(t) e^{-i\omega t} \right|^2, \quad (5.15)$$

where P denotes the power of the temporal window $v(t)$:

$$P = \frac{1}{M} \sum_{t=1}^M |v(t)|^2. \quad (5.16)$$

Finally, the Welch estimation of PSD is determined by averaging the windowed periodograms in Eq. 5.15:

$$\hat{\phi}_W(\omega) = \frac{1}{S} \sum_{j=1}^S \hat{\phi}_j(\omega) \quad (5.17)$$

The variance of the estimated PSD is decreased by allowing overlap between the data segments which leads to more periodograms to be averaged. Besides, by introducing the window in the periodogram computation it may be hoped to get more control over the bias of the estimated PSD by suppressing the side-lobe level. Furthermore, the temporal window may be used to give less weight to the data samples at the ends of each subsample, hence making the consecutive subsample sequences less correlated to one another, even though they are overlapping.

The Welch estimator can be efficiently computed via the fast Fourier transform (FFT), and is one of the most frequently used PSD estimation methods. In this work, Welch's method is used to estimate the PSD of GPS time series.

Chapter 6

Simulations

Before we test the capability of VADASE time series for normal modes detection, several simulations have been done on synthetic waveforms to investigate the influence of noise level, sampling rate, time series length, window size and overlapping rate of Welch's method, as well as the influence of stacking.

6.1 Synthetic time series

6.1.1 Principle

The displacement at any point on the surface of the Earth can be considered as a sum of discrete normal modes excited by some strong seismic motion, usually an earthquake. Earthquakes are typically of relatively short duration. After that, the Earth is in free oscillation. Away from the immediate vicinity of the earthquake, the motions of the Earth are small in amplitude and the total displacement at a recording site can be written as a sum of decaying cosinusoids:

$$u(t) = \sum_k A_k \cos(\omega_k t + \phi_k) e^{-\alpha_k t}, Q_k = \frac{\omega_k}{2\alpha_k} \quad (6.1)$$

where ω_k and α_k are the frequency and decay rate of the k 'th mode respectively, which are dependent on the structure of the Earth. The initial amplitude A_k and the initial phase ϕ_k depend on the properties of the source of excitation. Q_k is called the "quality" of the mode.

In this thesis, we only choose 5 spheroidal fundamental modes (see, table 6.1) for the simulation. As for the toroidal modes, the principle is the same.

TABLE 6.1: Spheroidal fundamental spheroidal modes for simulation

Mode	Initial amplitude [mm]	Frequency [mHz]	Initial phase	Quality
${}_0S_8$	1	1.41351	$\pi/2$	337.4
${}_0S_9$	1	1.57828	$\pi/2$	332.8
${}_0S_{10}$	1	1.72647	$\pi/2$	327.9
${}_0S_{11}$	1	1.86242	$\pi/2$	322.1
${}_0S_{12}$	1	1.99037	$\pi/2$	315.2

The frequency and quality of the chosen modes are given by Masters and Widmer (1995). The initial phases of all modes are set to be $\pi/2$ for convenience because we are only interested in the frequency information.

6.1.2 Signal-to-noise ratio

Signal-to-noise (SNR) is used to compare the level of a desired signal to the level of background noise. It is defined as the ratio of the power of a signal and the power of background noise. Since many signals have a very wide dynamic range, signals are often expressed using the logarithmic decibel scale. Based on the definition of decibel, signal-to-noise ratio can be expressed in decibels (dB) as:

$$\text{SNR}_{\text{dB}} = 10 \log_{10} \left(\frac{P_{\text{signal}}}{P_{\text{noise}}} \right) = 10 \log_{10} \left[\left(\frac{A_{\text{signal}}}{A_{\text{noise}}} \right)^2 \right] = 20 \log_{10} \left(\frac{A_{\text{signal}}}{A_{\text{noise}}} \right), \quad (6.2)$$

where P_{signal} and P_{noise} denote the average power of signal and noise, respectively. A_{signal} and A_{noise} are the amplitude of signal and noise.

In this thesis, 4 different levels of white Gaussian noise, -20 dB, -10 dB, 0 dB, 20 dB, are added to the original synthetic time series. Because the amplitude of normal modes are usually less than 1 mm while the accuracy of the VADASE time series is 1 cm to 2 cm, the smallest SNR is chosen to be -20 dB according to eqn. (6.2). The synthetic vertical displacements of the original time series and the time series with different levels of noise are shown in 6.1.

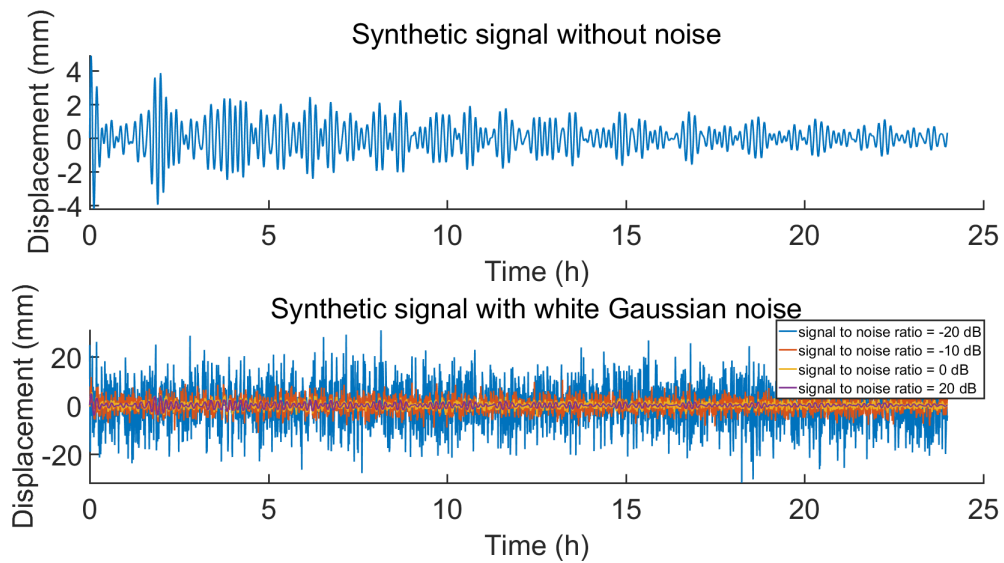


FIGURE 6.1: Vertical displacements of synthetic time series

6.2 Welch's PSD estimation in Matlab

The Welch PSD estimation is applied to the synthetic time series in Matlab using the `pwelch` function.

The syntax we use here is:

$$[p_{xx}, f] = \text{pwelch}(x, \text{window}, \text{noverlap}, \text{nfft}, f_s) \quad (6.3)$$

- p_{xx} is the estimated PSD, the units of the estimated PSD are in squared magnitude units of the time series data per unit frequency;
- f is the cyclical frequency, which is dependent on the sampling rate f_s because of the Nyquist sampling theorem;
- x is the input time series;
- `window` defines the type and length of window. `pwelch` divides the input time series x into overlapping segments of length equal to the length of window, and then multiplies each segment with the specified window;
- `noverlap` is the number of overlapped samples, specified as a positive integer smaller than the length of window;
- `nfft` is the number of DFT points, if the `nfft` is greater than the segment length, the data is zero-padded;

- f_s is the number of samples per unit time. If the unit of time is seconds, then the sample rate has units of Hz.

The purpose of the window function is to reduce the side-lobe level in the spectral density estimate, at the expense of frequency resolution. Here, the Hamming window is applied to give less weight to the data sample at the beginnings and the ends of each segment.

6.3 Simulation results and analyses

6.3.1 Different levels of SNR

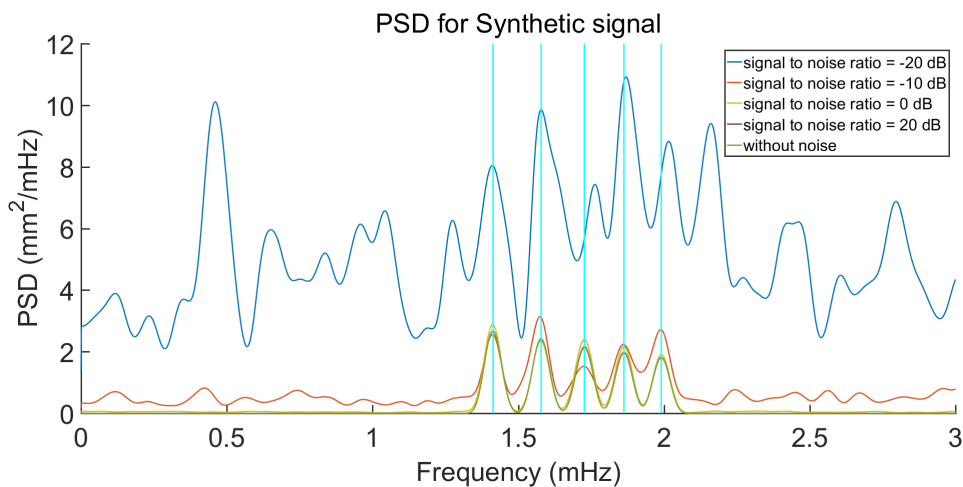


FIGURE 6.2: PSD of a signal with different noise levels on a single station
(the vertical cyan lines represent frequencies of the fundamental spheroidal modes based on the PREM model)

Figure 6.2 shows the PSD estimate of time series with different levels of SNR on a single station. The sampling rate and time series length are set as 30 s and 1 d. The Welch method is applied with 8 segments and 50% overlapping rate. Figure 6.2 clearly demonstrates that when SNR is less than -20 dB on a single station, some of the modes are buried by the noise and cannot be detected by the Welch method.

6.3.2 Effects of stacking of many stations

Although it is hard to detect all the desired fundamental modes on a single station, the stacked PSD of different stations truly improves the detection capability. Figure 6.3 shows the stacked PSD of 100 stations, where all the parameters are the same as those in subsection 6.3.1. In this case, it is clearly able to find the peaks of all desired modes, even if the SNR is -20 dB. The

noise is reduced not only in the stacking in time domain (divided segments in Welch's method), but also the stacking in space domain (100 stations).

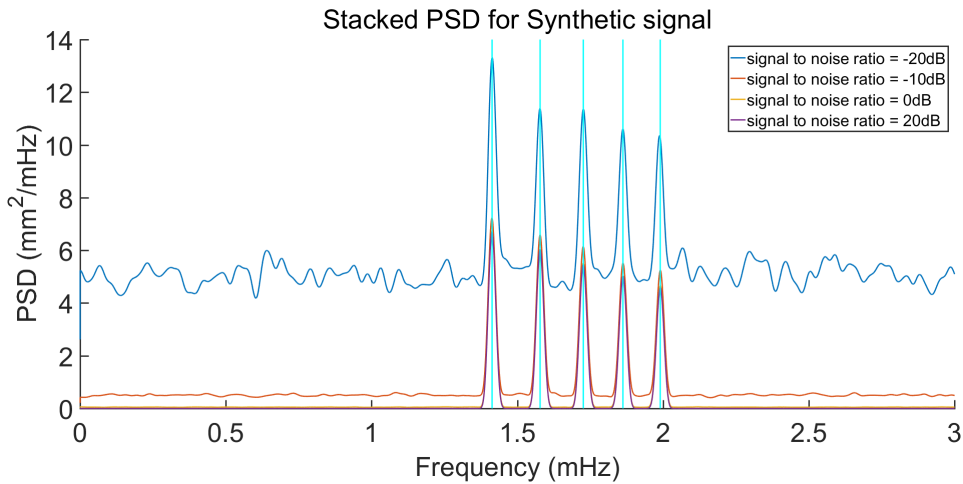


FIGURE 6.3: Stacked PSD of 100 stations

6.3.3 Different window size and overlap

In this section, the effects of window size and overlapping rate will be discussed. For convenience, only the time series of 1 d length is considered, with a sampling rate of 30 s and a SNR of -20 dB.

Figure 6.4 demonstrates how the window size influences the spectral resolution. Since the number of segments increases, the window size is decreasing, which leads to a poor resolution in spectral domain. As it is shown in figure 6.4, only ${}_0S_8$ and ${}_0S_9$ can be detected when there are 11 segments because of the loss of resolution.

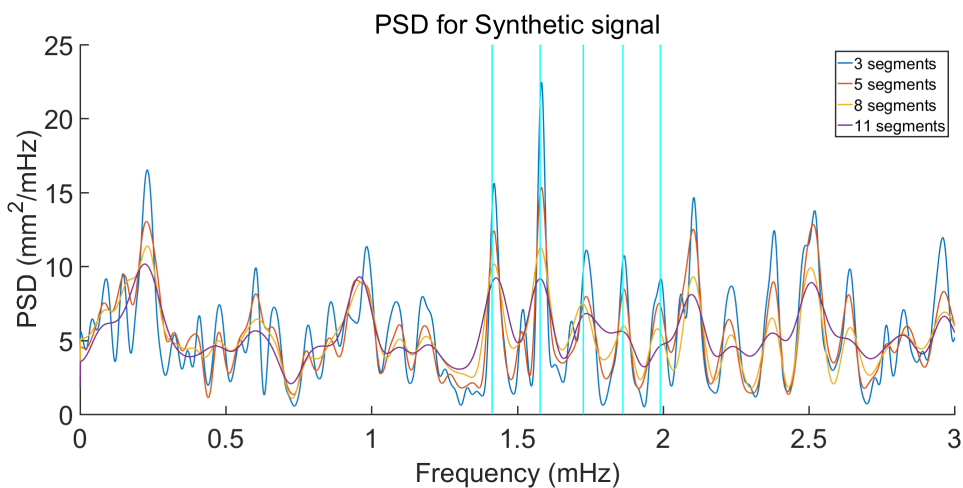


FIGURE 6.4: Effects of window size

Overlap between the data segments leads to more periodograms to be averaged, which can efficiently decrease the variance of the estimated PSD. Empirically, the overlapping rate should be set as 50% to get the most use

of data samples. When the overlapping rate is low, the data samples at the edges do not contribute as much as samples in the middle since the window function is close to zero at its edges. Although a overlapping rate higher than 50% gives more averages, no extra information is added since the same points are used for many times.

6.3.4 Different sampling rate and time series length

Both the change of sampling rate and time series length lead to a changing number of data samples. Typically, the Welch method will be more precise if more data are used for averaging. However, the influence of sampling rate and time series length is slightly different. Figure 6.5 shows the PSD on a single station of a 1 d length time series with a sampling rate of 1 s. The parameters of Welch's method are the same as in subsection 6.3.1. Comparing figure 6.5 and 6.2, all fundamental modes can be detected even for the SNR of -20 dB when the sampling rate is 1 s. It is worth to mention that the sampling rate should be larger than the highest frequency of desired modes, otherwise the PSD would be influenced by the aliasing effect.

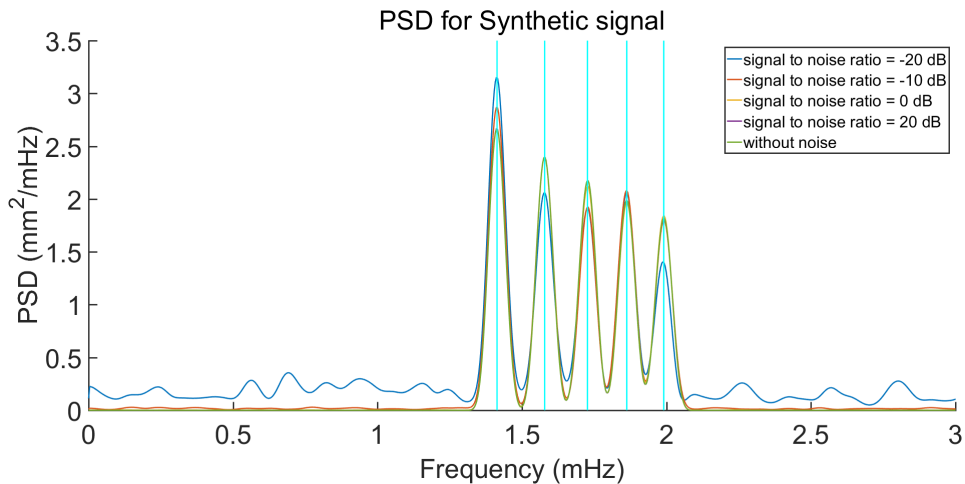


FIGURE 6.5: PSD of on a single station (length: 1 d; sampling rate: 1 s)

If the number of subsegment is fixed, the increase of time series length can improve the capability of normal modes detection by increasing the spectral resolution ($\Delta f = \frac{1}{T_{sub}}$). In our case, the smallest difference between the fundamental modes is 0.089 mHz, which means the length of subsegment should be at least 3.12 h.

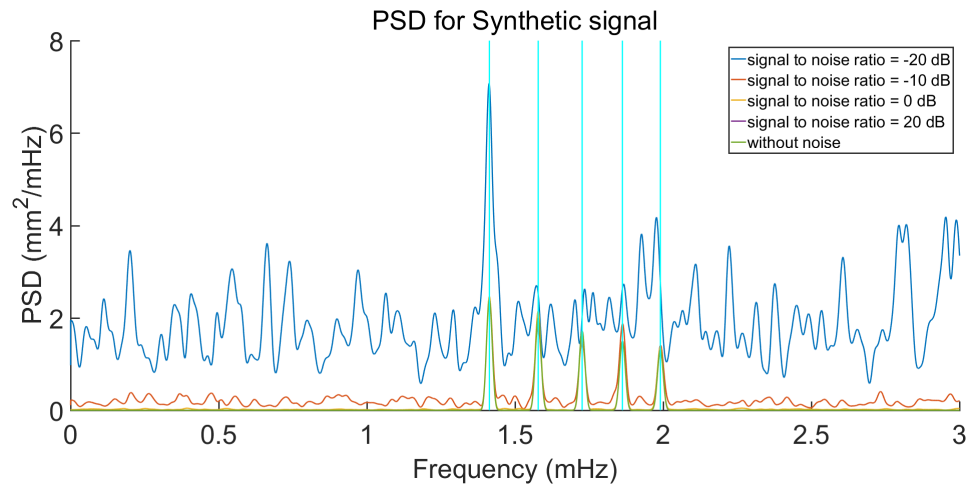


FIGURE 6.6: PSD of on a single station (length: 3 d; sampling rate: 30 s)

Chapter 7

Experiments on real VADASE time series

After the discussion of the influence of noise, sampling rate, time series length, window size and overlapping rate, as well as stacking in last chapter, the PSD estimate for the real VADASE time series is computed and stacked to detect the fundamental spheroidal and toroidal modes excited after the Tohoku earthquake (USGS $M_w = 9.0$, March 11, 2011, 05:46:24 UTC).

7.1 Data source

The VADASE velocity time series (referred to a local system, East, North and vertical) used in this chapter are provided by Mr. Giorgio with a length of 1 d and a sampling rate of 30 s. There are 126 stations in total from IGS and PBO network. Most of them are located around the Pacific Ocean, while roughly 30 stations are on the western coast of the United States (as shown in figure 7.1). The average RMSE of all the stations in the three direction are 0.018 m, 0.020 m, 0.043 m. The time series begin at March 12, 2011, 0:00:00 UTC, the day after the Tohoku earthquake. Cubic spline interpolation is applied to deal with missing epochs of some stations. If the missing solutions are larger than 5 min, the time series are chopped into two sub-series.

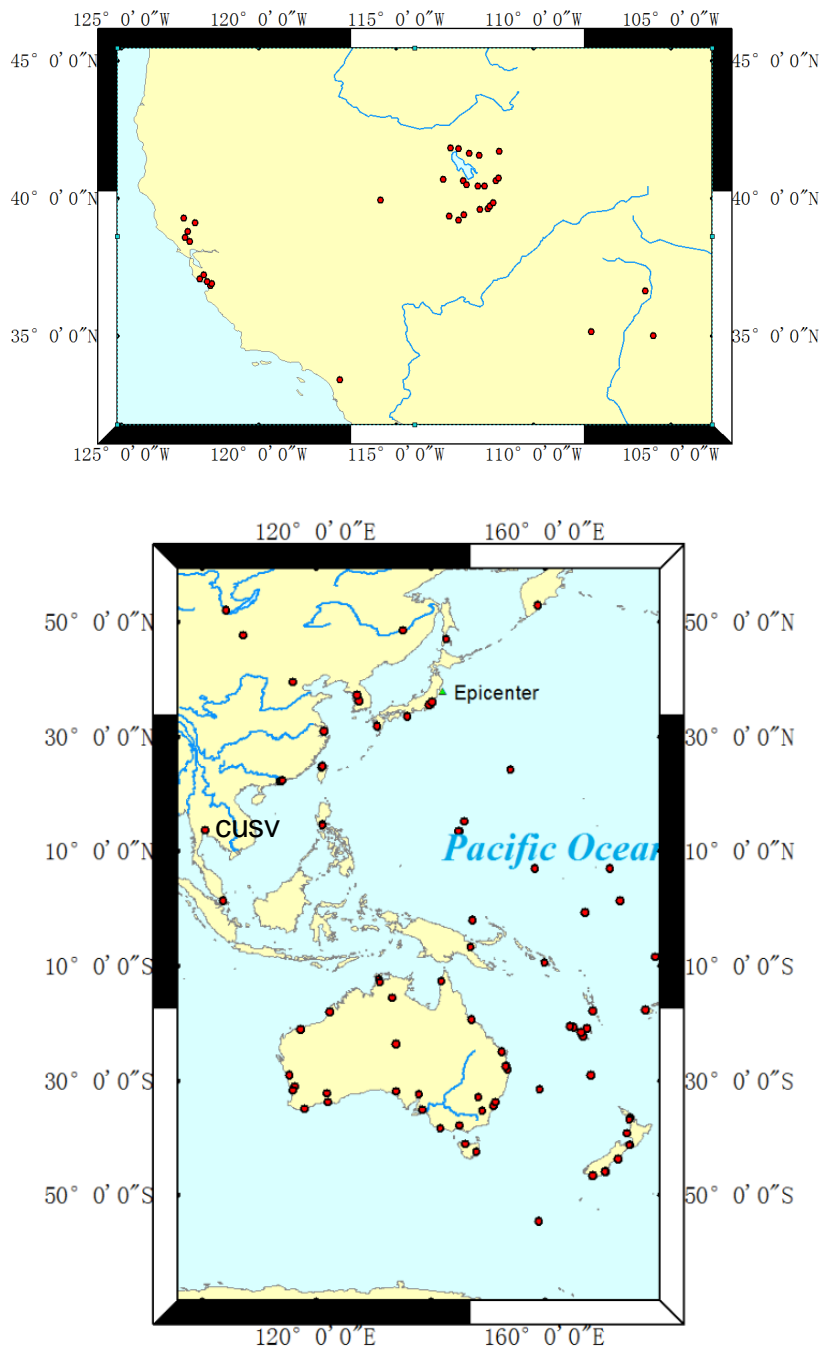


FIGURE 7.1: Distribution of stations

7.2 Estimated PSD with Welch's method

After cubic spline interpolation, the velocity time series are transformed from the time domain to the frequency domain via Welch's PSD estimate. Since the signal used here are velocity time series, no particular time series pre-processing such as detrending has been done.

The window size of Welch's method is the samples of 10 h ($\Delta f = \frac{1}{10 \times 60 \times 60} = 0.028$ mHz), which insures the target fundamental modes can be detected. The overlapping rate is 50%.

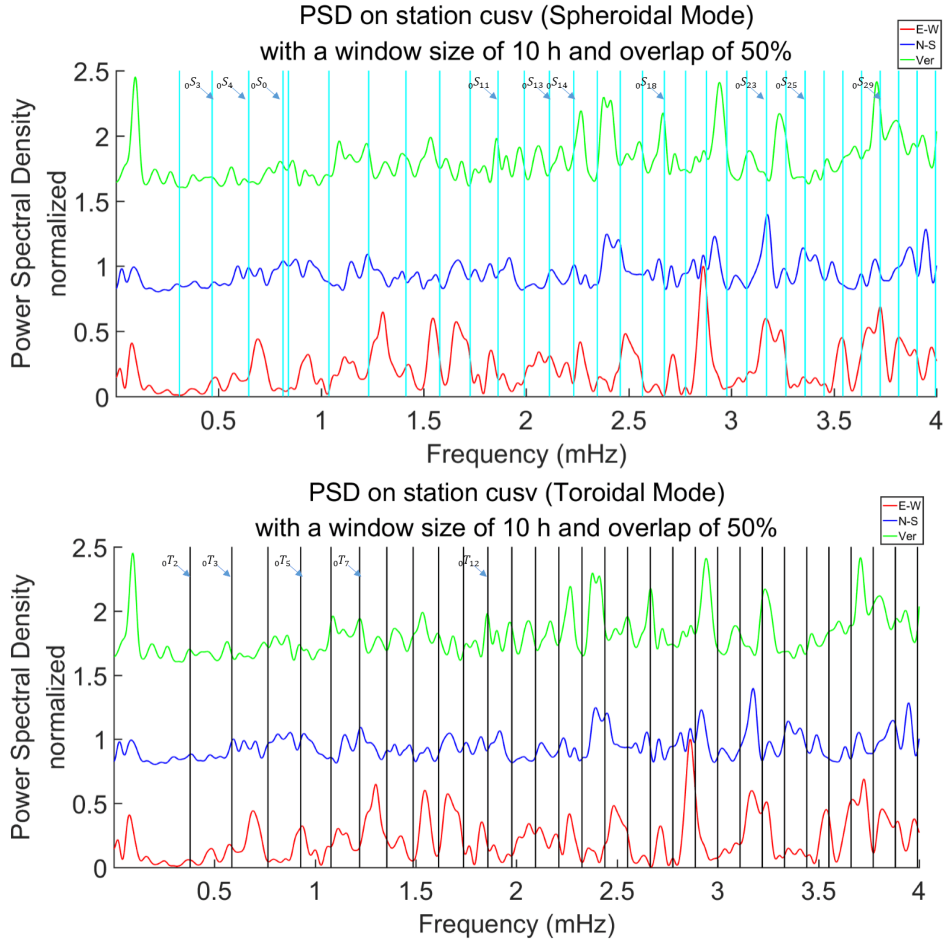


FIGURE 7.2: PSD of VADASE time series on a single station

First, the PSD of VADASE time series on station “cusv” are shown in figure 7.2. Station “cusv” is chosen here because the average SNR is the highest among all stations (-17 dB in E-W direction, -18 dB in N-S direction, -20 dB in vertical direction).

In figure 7.2, the cyan vertical lines represent the spheroidal fundamental modes ${}_0S_n$ with $0 \leq n \leq 32$ and the black vertical lines represent the toroidal fundamental modes ${}_0T_n$ with $1 \leq n \leq 31$. The red lines, blue lines and green lines represent the PSD estimates of E-W component, N-S component and vertical component, respectively. The PSD estimates are normalized in order to focus on the peaks. The N-S and the vertical components are shifted by a constant term (0.8 for the N-S and 1.6 for the vertical component) in order to avoid the overlapping of the three components. In this figure, we are able to identify only few spheroidal fundamental modes (${}_0S_n$

with $n = 0, 3, 7, 13, 18, 23, 25, 29$) and toroidal fundamental modes (${}_0T_n$ with $n = 2, 3, 5, 7$). Compared with figure 6.2, it corresponds to the conclusion that some fundamental modes are not detectable when the SNR is too small.

Then the stacking method is applied trying to lift the fundamental modes signal out of noise. The graphic is shown below. The N-S and vertical components are also shifted.

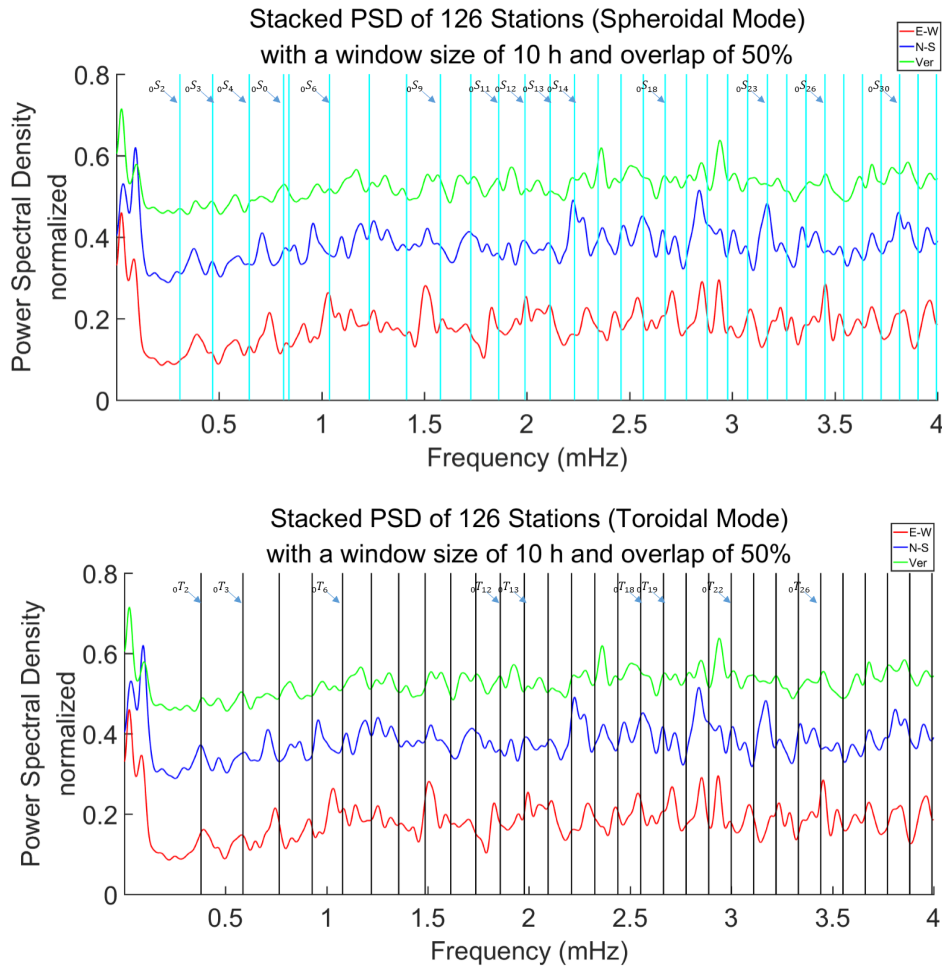


FIGURE 7.3: Stacked PSD of VADASE time series of 126 stations

It is clear that more fundamental modes (${}_0S_n$ with $n = 0, 2, 3, 4, 6, 9, 11, 12, 13, 18, 22, 26, 30$; ${}_0T_n$ with $n = 2, 3, 6, 13, 14, 17, 19, 22, 26$) are identical after the PSD estimates are stacked among all the stations. This proves the potential of the stacking method to illuminate the normal modes of the Earth, although some other modes are still not detectable.

It is worth to mention that the spheroidal modes should appear in both horizontal and vertical components while the toroidal modes principally appear in horizontal components.

7.3 Conclusion

Figure 7.3 summarizes our main results. The graphic represents the stacked PSD estimates obtained with the Welch method. Despite the fact that not all the fundamental modes are visible in the spectral domain, the VADASE time series show the capability of detecting normal modes of the Earth with the help of stacking method.

Comparing our results with the work of Mitsui and Heki (2012), we can conclude that less fundamental modes are detected and the accuracy of the detected peaks is worse in our works. There are several reasons leading to this difference (see table 7.1).

TABLE 7.1: Difference between Mitsui and Heki’s work and our work

	Mitsui and Heki’s work	our work
Data source	GEONET	IGS,PBO
Station	341 around Japan	126 all around the world
Time interval	6:00 on 11 March to 0:00 on 12 March	0:00 on 12 March to 0:00 on 13 March
Strategy	Kinematic PPP	VADASE

First of all, the data sources are different. In our work, the 126 stations used to compute the PSD estimates are from IGS and PBO, and they are located all around the world. By contrast, Mitsui uses 341 GEONET stations which are mainly located in Japan, close to the epicenter.

In Mitsui and Heki’s work, they applied the PPP strategy to compute the time series, which resulted in an accuracy level of mm. However, the accuracy of VADASE strategy only reaches to cm level, which is much higher than the amplitude of normal modes. Figure 7.4 shows that the signal-to-noise ratios (according to eqn. 6.2) of all the 126 mainly range from -40 dB to -30 dB, which is not sufficient to detect the buried signals. It is also worth to note that the signal-to-noise ratios vary in different direction. That is the reason that some modes are only detectable in horizontal or vertical component. Besides, the noise in reality is not only the white noise, but also the coloured noise whose PSD is not a constant in the spectral domain.

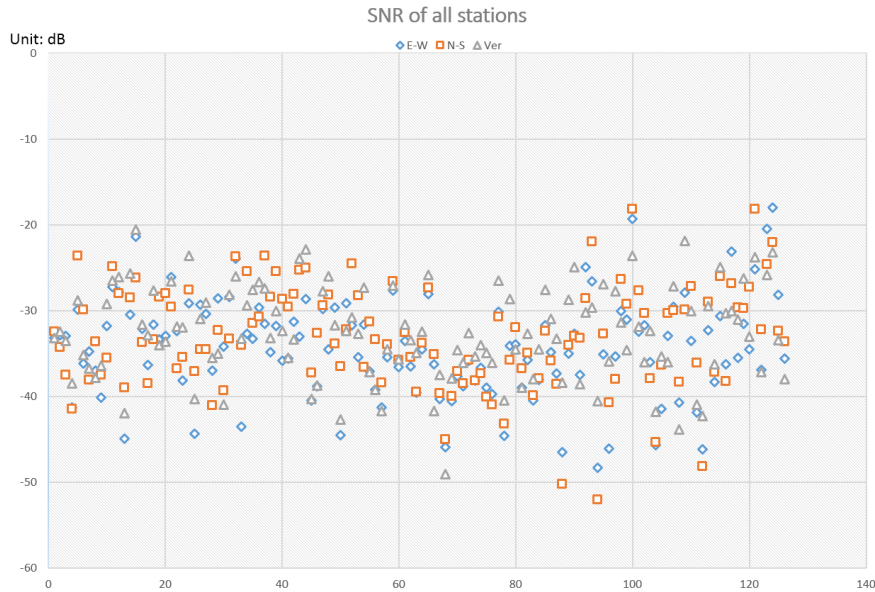


FIGURE 7.4: SNR of 126 stations in three directions

The stacking effects for time series with SNR of -30 dB and -40 dB are investigated using the synthetic data in last section. As is shown in figure 7.5, the normal modes are still visible for the time series with SNR of -30 dB. When the SNR decreases to -40 dB, most of the modes are buried by the noise and are not detectable. It is worth to note that the amplitude of PSD with SNR of -30 dB is about 10 times of that of PSD with SNR of -40 dB. For this reason, the amplitude are normalized to focus on the peaks.

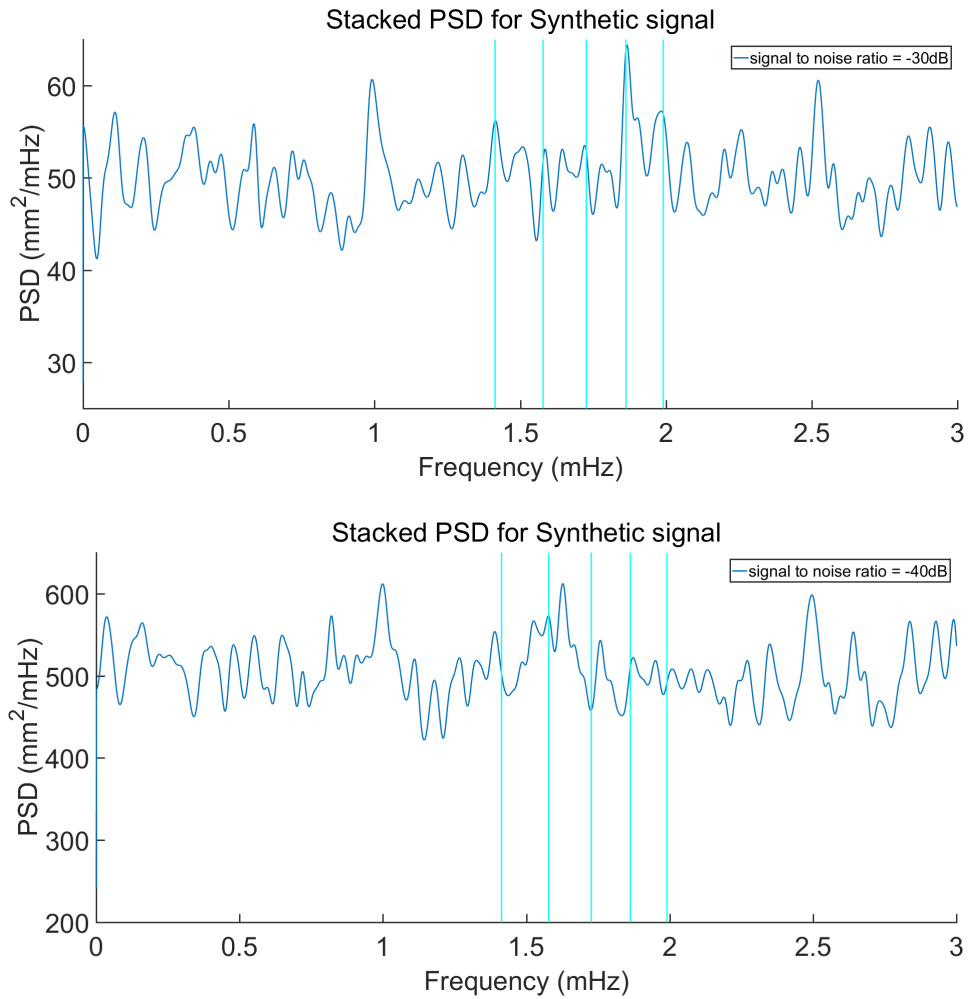


FIGURE 7.5: Stacked PSD of data with SNR of -30 dB and 40 dB

The time series lengths are also different. The time series used in Mitsui's work start from March 11, 2011, 06:00:00 UTC, few minutes after the main shock of the Tohoku earthquake. While our time series begin at March 12, 2011, 00:00:00 UTC, the day after the earthquake. Since the normal modes of the Earth decay with time, the modes are harder to detect because the amplitude is relatively small.

Appendix A

Ionosphere-free linear combination

Linear combinations of the original carrier phase or pseudorange observations are often used in order either to eliminate systematic biases (e.g. ionosphere-free combination) or to facilitate parameters estimation (e.g. geometry free combination to estimate the ionospheric models).

These linear combinations can be formed using as input any different level of the original observations. The main drawback of the linear combinations is that the noise of the observable is higher than the original ones. The formulation of the generic linear combination reads as:

$$L_{LC} = \alpha L_i + \beta L_j, \quad (\text{A.1})$$

where α and β are the real coefficients of the combination; L_i and L_j represent the original observations (either the pseudorange or the carrier phase) in length units with frequencies i and j respectively.

Ionosphere-free combination

The ionosphere-free combination is the most efficient method to eliminate the ionospheric delay by using two signals with different frequencies. This method can be thought of as the main reason for the GNSS signals to be broadcast with (at least) two different frequencies. The ionosphere-free combination is formed from equation A.1 using the following coefficients:

$$\alpha = \frac{f_i^2}{f_i^2 - f_j^2} \quad \beta = \frac{-f_j^2}{f_i^2 - f_j^2}$$

which have the property that $\alpha + \beta = 1$. To show the effectiveness of this method in removing the ionospheric delay, let write the carrier phase observation equation for the two frequencies (dependence on t is omitted):

$$L_1 = \rho_r^s + c(\delta t_r - \delta t^s) + T_r^s - I_{1r}^s + \lambda_1 N_{1r}^s; L_2 = \rho_r^s + c(\delta t_r - \delta t^s) + T_r^s - I_{2r}^s + \lambda_2 N_{2r}^s, \quad (\text{A.2})$$

here we notice that the terms that changes with the frequency are the ionospheric delay, λ and N . According to Eq. A.1, we have:

$$L_3 = (\alpha + \beta)[\rho_r^s + c(\delta t_r - \delta t^s) + T_r^s] - \alpha I_{1r}^s - \beta I_{2r}^s + \alpha \lambda_1 N_{1r}^s + \beta \lambda_2 N_{2r}^s. \quad (\text{A.3})$$

Expressing the two ionospheric delays with the TEC term, they became:

$$I_{1r}^s = \frac{\text{ATEC}}{f_{L1}^2} \quad I_{2r}^s = \frac{\text{ATEC}}{f_{L2}^2} \quad (\text{A.4})$$

Substituting this two equations into Eq. A.3, the two terms of the ionospheric delay are eliminated. According with the property $\alpha + \beta = 1$, we obtain the final equation of the ionosphere-free combination:

$$L_3 = \rho_r^s + c(\delta t_r - \delta t^s) + T_r^s + \alpha \lambda_1 N_{1r}^s + \beta \lambda_2 N_{2r}^s. \quad (\text{A.5})$$

Bibliography

- Alsop, LE et al. (1961). "Free oscillations of the earth observed on strain and pendulum seismographs". In: *Journal of Geophysical Research* 66.2, pp. 631–641.
- Backus, George and Freeman Gilbert (1961). "The rotational splitting of the free oscillations of the earth". In: *Proceedings of the National Academy of Sciences* 47.3, pp. 362–371.
- Bancroft, Stephen (1985). "An algebraic solution of the GPS equations". In: *IEEE Transactions on Aerospace and Electronic Systems* 1, pp. 56–59.
- Bartlett, MS (1948). "Smoothing periodograms from time series with continuous spectra". In: *Nature* 161.4096, pp. 686–687.
- (1950). "Periodogram analysis and continuous spectra". In: *Biometrika* 37.1/2, pp. 1–16.
- Benioff, Hugo et al. (1959). "Searching for the Earth's free oscillations". In: *Journal of Geophysical Research* 64.9, pp. 1334–1337.
- Benioff, Hugo et al. (1961). "Excitation of the free oscillations of the earth by earthquakes". In: *Journal of Geophysical Research* 66.2, pp. 605–619.
- Bilich, Andria et al. (2008). "GPS seismology: Application to the 2002 Mw 7.9 Denali fault earthquake". In: *Bulletin of the Seismological Society of America* 98.2, pp. 593–606.
- Blewitt, Geoffrey et al. (2009). "GPS for real-time earthquake source determination and tsunami warning systems". In: *Journal of Geodesy* 83.3-4, pp. 335–343.
- Bock, Yehuda et al. (2000). "Instantaneous geodetic positioning at medium distances with the Global Positioning System". In: *Journal of Geophysical Research: Solid Earth* 105.B12, pp. 28223–28253.
- Bolt, BA and Antonio Marussi (1962). "Eigenvibrations of the Earth observed at Trieste". In: *Geophysical Journal International* 6.3, pp. 299–311.
- Branzanti, Mara et al. (2013). "GPS near-real-time coseismic displacements for the great Tohoku-oki earthquake". In: *IEEE Geoscience and Remote Sensing Letters* 10.2, pp. 372–376.
- Dach, Rolf et al. (2007). "Bernese GPS software version 5.0". In: *Astronomical Institute, University of Bern* 640, p. 114.
- Dahlen, FA (1968). "The normal modes of a rotating, elliptical Earth". In: *Geophysical Journal International* 16.4, pp. 329–367.

- Dahlen, FA (1969). "The normal modes of a rotating, elliptical earth—II Near-resonance multiplet coupling". In: *Geophysical Journal International* 18.4, pp. 397–436.
- Dziewonski, AM and Don L Anderson (1981). "Preliminary reference Earth model". In: *Physics of the earth and planetary interiors* 25.4, pp. 297–356.
- Dziewonski, AM and F Gilbert (1972). "Observations of normal modes from 84 recordings of the Alaskan earthquake of 1964 March 28". In: *Geophysical Journal International* 27.4, pp. 393–446.
- Ge, Linlin (1999). "GPS seismometer and its signal extraction". In: *Proc. 12th Int. Tech. Meeting of the Satellite Division of the US Inst. of Navigation GPS ION'99*.
- Grewal, MS et al. (2007). *Global positioning systems, inertial navigation, and integration*. John Wiley & Sons.
- Herring, TA and KW Hudnut (1993). "Detection of crustal deformation from the Landers earthquake sequence using continuous geodetic measurements". In: *Nature* 361, p. 28.
- Hofmann-Wellenhof, Bernhard et al. (2007). *GNSS—global navigation satellite systems: GPS, GLONASS, Galileo, and more*. Springer Science & Business Media.
- Jordan, TH (1978). "A procedure for estimating lateral variations from low-frequency eigenspectra data". In: *Geophysical Journal International* 52.3, pp. 441–455.
- Kelvin, Lord (1863). "Dynamical Problem Regarding Elastic Spheroid Shell; On the Rigidity of the Earth". In: *Phil. Trans. Roy. Soc. London, Treatise on Natural Philosophy* 2, p. 837.
- Kobayashi, Naoki and Kiwamu Nishida (1998). "Continuous excitation of planetary free oscillations by atmospheric disturbances". In: *Nature* 395.6700, pp. 357–360.
- Larson, KM (2009). "GPS seismology". In: *Journal of Geodesy* 83.3-4, pp. 227–233.
- Liljequist, GH and Konrad Cehak (2013). *Allgemeine Meteorologie*. Springer-Verlag.
- Lognonné, Philippe (1989). "Modélisation des modes propres de vibration dans une Terre anélastique en hétérogène: théorie et applications". PhD thesis. Paris 7.
- (1991). "Normal modes and seismograms in an anelastic rotating Earth". In: *Journal of Geophysical Research: Solid Earth* 96.B12, pp. 20309–20319.
- Lognonné, Philippe and Eric Clévéde (2002). "Normal modes of the earth and planets". In: *International Geophysics* 81, pp. 125–I.
- Love, AEH (1911). *Some Problems of Geodynamics*.

- Madariaga, Raul and Keiiti Aki (1972). "Spectral splitting of toroidal-free oscillations due to lateral heterogeneity of the Earth's structure". In: *Journal of Geophysical Research* 77.23, pp. 4421–4431.
- Masters, Guy and Freeman Gilbert (1981). "Structure of the inner core inferred from observations of its spheroidal shear modes". In: *Geophysical Research Letters* 8.6, pp. 569–571.
- Masters, Guy et al. (1982). "Aspherical Earth structure from fundamental spheroidal-mode data". In: *Nature* 298.5875, pp. 609–613.
- Masters, TG and R Widmer (1995). "Free oscillations: frequencies and attenuations". In: *Global Earth Physics: a handbook of physical constants* 1, p. 104.
- McCarthy, DD and Gérard Petit (2003). "Iers technical note no. 32". In: *IERS Conventions* 1.32, pp. 33–56.
- Mendiguren, JA (1973). "Identification of free oscillation spectral peaks for 1970 July 31, Colombian deep shock using the excitation criterion". In: *Geophysical Journal International* 33.3, pp. 281–321.
- Mitsui, Yuta and Kosuke Heki (2012). "Observation of Earth's free oscillation by dense GPS array: After the 2011 Tohoku megathrust earthquake". In: *Scientific reports* 2, p. 931.
- Nawa, Kazunari et al. (1998). "Incessant excitation of the Earth's free oscillations". In: *Earth Planets Space* 50, pp. 3–8.
- Ness, NR et al. (1961). "Observation of the free oscillation of the earth". In: *J Geophys Res* 66.2, pp. 621–629.
- Nikolaidis, RM et al. (2001). "Seismic wave observations with the Global Positioning System". In: *Journal of Geophysical Research* 106.21,897.
- Rayleigh, John (1896). *The theory of sound*. Vol. 2. Macmillan.
- Romanowicz, Barbara (1990). "The upper mantle degree 2: constraints and inferences from global mantle wave attenuation measurements". In: *Journal of Geophysical Research: Solid Earth* 95.B7, pp. 11051–11071.
- (1994). "Anelastic tomography: A new perspective on upper mantle thermal structure". In: *Earth and Planetary Science Letters* 128.3-4, pp. 113–121.
- Roult, G et al. (1990). "3-D upper mantle shear velocity and attenuation from fundamental mode free oscillation data". In: *Geophysical Journal International* 101.1, pp. 61–80.
- Saastamoinen, J (1972). "Atmospheric correction for the troposphere and stratosphere in radio ranging satellites". In: *The use of artificial satellites for geodesy*, pp. 247–251.
- Silver, PG and TH Jordan (1981). "Fundamental spheroidal mode observations of aspherical heterogeneity". In: *Geophysical Journal International* 64.3, pp. 605–634.
- Stoica, Petre, Randolph L Moses, et al. (2005). *Spectral analysis of signals*. Vol. 452. Pearson Prentice Hall Upper Saddle River, NJ.

- Suda, Naoki et al. (1998). "Earth's background free oscillations". In: *Science* 279.5359, pp. 2089–2091.
- Valette, Bernard (1986). "About the influence of pre-stress upon adiabatic perturbations of the Earth". In: *Geophysical Journal International* 85.1, pp. 179–208.
- (1987). "Spectre des oscillations libres de la Terre: aspects mathématiques et géophysiques". PhD thesis. Paris 6.
- Welch, Peter (1967). "The use of fast Fourier transform for the estimation of power spectra: a method based on time averaging over short, modified periodograms". In: *IEEE Transactions on audio and electroacoustics* 15.2, pp. 70–73.
- Woodhouse, JH (1980). "The coupling and attenuation of nearly resonant multiplets in the Earth's free oscillation spectrum". In: *Geophysical Journal International* 61.2, pp. 261–283.
- Woodhouse, JH and FA Dahlen (1978). "The effect of a general aspherical perturbation on the free oscillations of the Earth". In: *Geophysical Journal International* 53.2, pp. 335–354.
- Zharkov, BN and VM Lyubimov (1970a). "Theory of spheroidal vibrations for a spherically asymmetric model of the Earth". In: *Iz. Acad. Sci., USSR, Phys. Solid Earth* 10, pp. 613–618.
- (1970b). "Torsional oscillations of a spherically asymmetrical model of the Earth". In: *Bull.(Zzu.) Akad. Sci. USSR, Earth Physics*.